Towards improved knowledge of the vertical distribution of aerosols in the atmosphere: part I

BARBARA SCHERLLIN-PIRSCHER

Chemical Weather Forecasts
Division Data, Methods, Models
Zentralanstalt für Meteorologie und Geodynamik (ZAMG)
Hohe Warte 38, 1190 Vienna, Austria

Final project report

Developmental Testbed Center (DTC) Visitor Program

AUGUST 2019

Contents

Acknowledgements

1. Introduction

The presence and distribution of atmospheric aerosols have a strong impact on the Earth's system. Interactions with meteorological parameters through radiative effects and cloud formation, for example, significantly affect the Earth's weather and climate. During airborne hazard events, such as volcanic eruptions, forest fires, or sand storms, the amount of aerosols in the atmosphere significantly increases, affecting also air quality and human health.

Numerical model applications help to understand the dispersion of aerosols. Dispersion modeling and chemical transport modeling, however, remain challenging due to large uncertainties of source terms, chemical conversions, and atmospheric transport processes.

Air quality modeling relies on the adequate representation of the initial aerosol distribution. Uncertainties of initial aerosol fields can be reduced by data assimilation, which combines information of observations with numerical model output. In recent years, substantial progress has been achieved in assimilating aerosol-related quantities into dispersion models (e.g., Yumimoto et al., 2008; Zhang et al., 2008; Benedetti et al., 2009; Liu et al., 2011; Zhang et al., 2011; Schwartz et al., 2012; Pagowski et al., 2014; Sič et al., 2016) either using a 3-Dimensional Variational (3DVar), 3DVar First Guess at Appropriate Time (FGAT), or 4-Dimensional Variational (4DVar) data assimilation system. All studies revealed noticeable improvements of model forecasts after assimilating aerosol-related observations.

Most assimilated observations are either surface measurements or measurements of vertically integrated quantities such as Aerosol Optical Depth (AOD). The missing vertical information of these measurements inhibits any change of the vertical profile shape but multi-day data assimilation allows modifications of the profile shape due to interactions with meteorological conditions (Sič et al., 2016). The assimilation of vertically-resolved measurements introduces direct information of the vertical profile from observations into the model. Recently, the assimilation of vertical LIght Detection And Ranging (LIDAR) measurements revealed a promising and coherent impact in air quality modeling studies (e.g., Yumimoto et al., 2008; Sič, 2014; Wang et al., 2014; Geisinger et al., 2017).

The aim of this visiting scientist project was to implement LIDAR data assimilation into the Gridpoint Statistical Interpolation (GSI) 3DVar because the assimilation of vertical LIDAR profiles will significantly improve the knowledge of the vertical distribution of aerosols, which is particularly important during natural hazard events such as volcanic eruptions or sand storms. It will help to improve the vertical aerosol representation in air quality forecasts.

1

2. Project description

The aim of the project was to implement LIDAR data assimilation into the GSI. The GSI is tightly coupled with the Community Radiative Transfer Model (CRTM). This model simulates satellite radiances that are needed to assimilate radiances from infrared and microwave sensors. It also includes the AOD observation operator (Liu et al., 2011). The assimilation of LIDAR-based quantities therefore requires both, the extension of the GSI and the CRTM.

Two one-month visits were planned for this project. Benjamin T. Johnson (Joint Center for Satellite Data Assimilation (JCSDA), University Corporation for Atmospheric Research (UCAR), National Oceanic and Atmospheric Administration (NOAA), College Park, MD, USA) and Mariusz Pagowski (Earth System Research Laboratory (ESRL), NOAA, Boulder, CO, USA) hosted me during these visits. I spent two weeks at NOAA in College Park, MD, and two weeks at NOAA in Boulder, CO, in March/April 2018 and focused on (i) getting detailed information about the CRTM and GSI, (ii) designing the implementation of LIDAR data assimilation, and (iii) starting its implementation as planned in the proposal.

Since it was clear from the beginning that the project would demand more work of concentrated effort, it was planned that parts of this work were also performed at my home institution Zentralanstalt für Meteorologie und Geodynamik (ZAMG) in Austria. Due to a lot of other commitments, however, the progress was slower than expected. I focused on the implementation of the observation operator in the CRTM. While it was straightforward to simulate aerosol extinction coefficients, the calculation of the backscattering coefficients was challenging and required a lot of effort.

During the second one-month research visit at ESRL, NOAA, in Boulder, CO, in fall 2018, I finalized the calculation of the backscattering coefficients and tested and evaluated the CRTM implementation. This report therefore contains information and results of modeling Aerosol Optical Properties (AOP) with CRTM only. It is planned that the implementation in the assimilation software tool will be done in a second part of this project.

3. Calculation of AOP with CRTM

CRTM is able to simulate AOD as observed by the Moderate Resolution Imaging Spectroradiometer (MODIS) instrument onboard the Aqua and Terra satellites (Liu et al., 2011). More recently, CRTM capabilities have been extended to simulate AOD measurements from the Visible Infrared Imaging Radiometer Suite (VIIRS) instrument onboard the joint National Aeronautics and Space Administration (NASA)/NOAA Suomi National Polar-orbiting Partnership (Suomi-NPP) satellite.

So far, CRTM only considers Global Ozone Chemistry Aerosol Radiation and Transport (GOCART) aerosols, which include hydrophobic and hydrophilic Organic Carbon (OC), hydrophobic and hydrophilic Black Carbon (BC), dust, sea salt, and sulfate. Information about aerosol radii, aerosol hygroscopic growth, and optical properties (such as mass extinction coefficients, single scatter albedo, and phase coefficients for aerosols) are available in a look-up table. In this study, an extended aerosol look-up table was created and used to simulate AOP from LIDAR measurements.

3.1. Physical basis

Radiation that passes through the atmosphere is scattered and absorbed by molecules and particles. Absorption and scattering therefore have molecular and aerosol contributions. Both quantities can be simulated with CRTM in general. However, I focus here on the description of aerosol-related effects and describe the calculation of AOD, aerosol extinction and backscattering coefficients.

Optical depth τ (dimensionless) of a layer containing an aerosol of a specific type i contains contributions of absorption and scattering and is calculated as

$$\tau(i, r_{\text{eff}}, \lambda) = \chi(i)\kappa_{\text{e}}(i, r_{\text{eff}}, \lambda), \tag{1}$$

where χ (in $\text{kg}\,\text{m}^{-2}$) is the integrated aerosol concentration of the layer and κ_{e} (in $\text{m}^2\,\text{kg}^{-1}$) is the mass extinction coefficient for the aerosol with effective radius r_{eff} at wavelength λ. Because CRTM computations are performed for height and thickness independent quantities, optical depth of a layer is the same as its volume extinction coefficient β_{e} (usually $\tau = \beta_{\text{e}}\mathrm{d}z$).

Considering all types of aerosols in a layer, total AOD and total volume extinction coefficient E are

$$\text{AOD}(\lambda) = E(\lambda) = \sum_{i=1}^{\text{n\_aerosols}} \tau(i, r_{\text{eff}}, \lambda) = \sum_{i=1}^{\text{n\_aerosols}} \chi(i)\kappa_{\text{e}}(i, r_{\text{eff}}, \lambda). \tag{2}$$

The volume scattering coefficient β_{s} (dimensionless) of an aerosol layer is

$$\beta_{\text{s}}(i, r_{\text{eff}}, \lambda) = \chi(i)\kappa_{\text{e}}(i, r_{\text{eff}}, \lambda)w(i, r_{\text{eff}}, \lambda), \tag{3}$$

where

$$w = \frac{\beta_{\text{s}}}{\beta_{\text{e}}} = \frac{\beta_{\text{s}}}{\beta_{\text{s}} + \beta_{\text{a}}} \tag{4}$$

is the dimensionless single scatter albedo. In a purely scattering medium, the volume absorption coefficient $\beta_a = 0$ and $w = 1$, in a purely absorbing medium $\beta_s = 0$ and $w = 0$. The volume scattering coefficient of all aerosols S is computed as

$$S(\lambda) = \sum_{i=1}^{\text{n\_aerosols}} \beta_s(i, r_{\text{eff}}, \lambda) = \sum_{i=1}^{\text{n\_aerosols}} \chi(i)\kappa_e(i, r_{\text{eff}}, \lambda)w(i, r_{\text{eff}}, \lambda). \tag{5}$$

The calculation of the volume backscattering coefficient of an aerosol layer requires knowledge of the scattering direction. This information is given in the phase coefficients c. The part that is backscattered by aerosols can be calculated by evaluating the function P at $x = -1$ because $x = \cos\varphi$ and $\varphi = \pi$ for backscattering. Clenshaw's recurrence formula can be used for this purpose. It can be shown that

$$P(x) = -\frac{1}{2}b_2(x) + xb_1(x) + c_0 \tag{6}$$

where b_1 and b_2 are calculated recursively and c_0 is the zeroth phase coefficient. Details are given in Appendix A. Mass backscattering coefficients κ_b are then obtained by

$$\kappa_b(i, r_{\text{eff}}, \lambda) = \kappa_e(i, r_{\text{eff}}, \lambda)\omega(i, r_{\text{eff}}, \lambda)\frac{P(i, r_{\text{eff}}, \lambda, \pi)}{4\pi}. \tag{7}$$

The volume backscattering coefficient is obtained from multiplying the mass backscattering coefficients with the integrated aerosol concentration

$$\beta_b(i, r_{\text{eff}}, \lambda) = \chi(i)\kappa_b(i, r_{\text{eff}}, \lambda) \tag{8}$$

and the volume backscattering coefficient of all aerosols is

$$\begin{aligned} B(\lambda) &= \sum_{i=1}^{\text{n\_aerosols}} \beta_b(i, r_{\text{eff}}, \lambda) \\ &= \sum_{i=1}^{\text{n\_aerosols}} \chi(i)\kappa_b(i, r_{\text{eff}}, \lambda) \\ &= \sum_{i=1}^{\text{n\_aerosols}} \chi(i)\kappa_e(i, r_{\text{eff}}, \lambda)\omega(i, r_{\text{eff}}, \lambda)\frac{P(i, r_{\text{eff}}, \lambda, \pi)}{4\pi}. \end{aligned} \tag{9}$$

The inverse of the last two terms of Eqs. (7) and (9) also refers to the LIDAR Ratio (LR) S

$$S(i, r_{\text{eff}}, \lambda) = \frac{4\pi}{w(i, r_{\text{eff}}, \lambda)P(i, r_{\text{eff}}, \lambda, \pi)}. \tag{10}$$

It depends on the aerosol phase function $P(\pi)$ and single scatter albedo w, and is therefore sensitive to the aerosol size, its shape, and refractive index (He et al., 2006). The LIDAR ratio is also known as the extinction-to-backscattering ratio that can be written as

$$S = \frac{\beta_e}{\beta_b} = \frac{\beta_a + \beta_s}{\beta_b}. \tag{11}$$

Several studies showed that the LIDAR ratio is not constant. However, a constant LIDAR ratio can be assumed to estimate the volume backscattering coefficient. For GOCART aerosols, the following reasonable values can be found in the literature

- Dust: $S_{\text{dust}} = 48$ (Burton et al., 2013)

- Sea salt: $S_{\text{sea salt}} = 22$ (Burton et al., 2013)

- Organic carbon: $S_{\text{OC}} = 65$

- Black carbon: $S_{\text{BC}} = 65$

- Sulfate: $S_{\text{sulf}} = 62$ (Prata et al., 2017)

Knowledge of volume extinction coefficients and the LIDAR ratio allows the estimation of volume backscattering coefficients

$$\beta_{\text{b}}(i, r_{\text{eff}}, \lambda) \approx \frac{\beta_{\text{e}}(i, r_{\text{eff}}, \lambda)}{S(i)}. \tag{12}$$

and the volume backscattering coefficient of all aerosols can be approximated as

$$B(\lambda) = \sum_{i=1}^{\text{n\_aerosols}} \beta_{\text{b}}(i, r_{\text{eff}}, \lambda) \approx \sum_{i=1}^{\text{n\_aerosols}} \frac{\beta_{\text{e}}(i, r_{\text{eff}}, \lambda)}{S(i)}. \tag{13}$$

An important step towards successfully modeling AOP with CRTM was the correct reconstruction of the backscattering coefficients. This has been done outside of the CRTM environment. For fast and easy access, resulting mass backscattering coefficients were then included in the CRTM aerosol look-up table for all aerosol types, pre-defined aerosol radii, and wavelengths.

3.2. Tangent linear and adjoint models

3.2.1. Theoretical background

Tangent linear and adjoint models are needed for variational data assimilation. The tangent linear model allows the computationally efficient estimation of the model trajectory. If M is a model that describes the model's trajectory, i.e.,

$$x(t_{i+1}) = M[x(t_i)], \tag{14}$$

the tangent linear model of M, called M' is

$$\delta x(t_{i+1}) = M'[x(t_i)]\delta x(t_i) = \frac{\partial M[x(t_i)]}{\partial x}\delta x(t_i). \tag{15}$$

M' is a first order approximation that describes the evolution of a perturbation δx of the control variable x (initial condition).

For any linear operator M' exists an adjoint operator $M^\star$ such that

$$\langle x, M'y \rangle = \langle M^\star x, y \rangle \tag{16}$$

where $\langle, \rangle$ is an inner product and x and y are vectors (or functions) of the space where the product is defined. In Euclidian space, the adjoint matrix is equal to the transposed matrix

$$M^\star = M'^{\mathrm{T}}. \tag{17}$$

The solution of the adjoint equations yields the gradient of the cost function at time t_i.

3.2.2. Example: Tangent linear and adjoint model of optical depth

In CRTM, optical depth is modeled as

$$\tau = \chi \kappa_{\mathrm{e}}, \tag{18}$$

with χ being the integrated aerosol concentration of a layer and κ_{e} the mass extinction coefficient, see also Section 3.1, Eq. (1). Because χ and κ_{e} are independent variables

$$
\begin{aligned}
\chi &= \chi \\
\kappa_{\mathrm{e}} &= \kappa_{\mathrm{e}} \\
\tau &= \chi \kappa_{\mathrm{e}}.
\end{aligned}
\tag{19}
$$

The first derivative of this set of equations (i.e., the tangent linear statement) is

$$
\begin{aligned}
\delta\chi &= \delta\chi \\
\delta\kappa_{\mathrm{e}} &= \delta\kappa_{\mathrm{e}} \\
\delta\tau &= \kappa_{\mathrm{e}}\delta\chi + \chi\delta\kappa_{\mathrm{e}}
\end{aligned}
\tag{20}
$$

or

$$
\begin{pmatrix} \delta\chi \\ \delta\kappa_{\mathrm{e}} \\ \delta\tau \end{pmatrix} = \begin{pmatrix} 1 & 0 & 0 \\ 0 & 1 & 0 \\ \kappa_{\mathrm{e}} & \chi & 0 \end{pmatrix} \begin{pmatrix} \delta\chi \\ \delta\kappa_{\mathrm{e}} \\ \delta\tau \end{pmatrix}
\tag{21}
$$

in matrix notation.

Since the adjoint matrix equals the transposed matrix in Euclidian space and

$$
\begin{pmatrix} 1 & 0 & 0 \\ 0 & 1 & 0 \\ \kappa_{\mathrm{e}} & \chi & 0 \end{pmatrix}^{\mathrm{T}} = \begin{pmatrix} 1 & 0 & \kappa_{\mathrm{e}} \\ 0 & 1 & \chi \\ 0 & 0 & 0 \end{pmatrix},
\tag{22}
$$

the adjoint model of τ can be written as

$$
\begin{pmatrix} \delta\chi^\star \\ \delta\kappa_{\mathrm{e}}^\star \\ \delta\tau^\star \end{pmatrix} = \begin{pmatrix} 1 & 0 & \kappa_{\mathrm{e}} \\ 0 & 1 & \chi \\ 0 & 0 & 0 \end{pmatrix} \begin{pmatrix} \delta\chi^\star \\ \delta\kappa_{\mathrm{e}}^\star \\ \delta\tau^\star \end{pmatrix},
\tag{23}
$$

which is equivalent to

$$
\begin{aligned}
\delta\chi^\star &= \delta\chi^\star + \kappa_{\mathrm{e}}\delta\tau^\star \\
\delta\kappa_{\mathrm{e}}^\star &= \delta\kappa_{\mathrm{e}}^\star + \chi\delta\tau^\star \\
\delta\tau^\star &= 0.
\end{aligned}
\tag{24}
$$

This set of equations describes the adjoint model of optical depth.

Tangent linear and adjoint models of the volume extinction coefficient, absorption coefficient, volume scattering coefficient, and volume backscattering coefficient are described in detail in Appendix B.

3.3. Aerosol scattering look-up tables

Aerosol scattering look-up tables contain information of relevant physical aerosol characteristics. The CRTM aerosol table is based on Hess et al. (1998) and Chin et al. (2000). SPHerical (SPH) particles were assumed. Aerosol size (effective radius, which depends on the amount of atmospheric humidity for most aerosol types), mass extinction coefficient, single scatter albedo, and the asymmetry parameter were made available for dust, sea salt (aerosols in Sea Salt Accumulation Mode (SSAM) and Sea Salt Coarse Mode (SSCM)), OC, BC, and sulfate. The CRTM aerosol table also contains phase coefficients, which were used to reconstruct the mass backscattering coefficients as described in detail in Appendix A. This variable was then added in an extended CRTM aerosol table.

The same aerosol properties can be computed with Modeled Optical Properties of enSeMbles of Aerosol Particles (MOPSMAP) (Gasteiger and Wiegner, 2018). This model also provides aerosol characteristics of non-spherical dust particles. Josef Gasteiger, University of Vienna, Austria, used this model and computed optical aerosol characteristics of GOCART aerosols and added information for two non-spherical dust aerosols Volume-Equivalent Prolate Spheriods (VEPS) and Cross-Section Equivalent Prolate Spheriods (CSEPS). Non-spherical VEPS have the same mass and volume as corresponding spherical particles. The aspect ratio of CSEPS was calculated after Kandler et al. (2009). Refractive indices of the MOPSMAP model were used from Hess et al. (1998).

The following sections give more detailed information about the content of the aerosol look-up tables from CRTM and MOPSMAP.

3.3.1. Effective radius

Log-normal size distributions were assumed for each aerosol type with

$$
n(\ln r) = \frac{N}{\sqrt{2\pi}}\frac{1}{\ln(\sigma_{\mathrm{g}})}\exp\left[-\frac{1}{2}\left(\frac{\ln r - \ln r_{\mathrm{g}}}{\ln(\sigma_{\mathrm{g}})}\right)^2\right],
\tag{25}
$$

and N being the number of particles within the mode, r the radius, r_{g} the geometric median radius, and σ_{g} the geometric mean standard deviation (Liu et al., 2011). The

k^{th} moment of the log-normal distribution (M_k) can be computed from (Binkowski and Roselle, 2003)

$$M_k = N r_{\text{g}}^k \exp\left[\frac{k^2}{2}\ln^2(\sigma_{\text{g}})\right] \tag{26}$$

so that

$$M_0 = N, \tag{27}$$

$$M_1 = N r_{\text{g}} \exp\left[\frac{1}{2}\ln^2(\sigma_{\text{g}})\right], \tag{28}$$

$$M_2 = N r_{\text{g}}^2 \exp\left[2\ln^2(\sigma_{\text{g}})\right], \tag{29}$$

$$M_3 = N r_{\text{g}}^3 \exp\left[\frac{9}{2}\ln^2(\sigma_{\text{g}})\right]. \tag{30}$$

The zeroth moment M_0 is the number of aerosol particles N, the second moment (M_2) is proportional to the total particulate surface area, and the third moment (M_3) is proportional to the particulate volume. Since the effective radius (r_{eff}) is defined as $r_{\text{eff}} = \frac{M_3}{M_2}$, it can be calculated as

$$r_{\text{eff}} = r_{\text{g}} \exp\left[\frac{5}{2}\ln^2(\sigma_{\text{g}})\right]. \tag{31}$$

The effective radius (in μm) is different for each aerosol type. Table 1 summarizes the range of radii covered by CRTM and MOPSMAP.

Furthermore the aerosol size of sea salt, hydrophilic OC and BC, and sulfate increases with ambient moisture. Hygroscopic growth rate of the CRTM look-up table is based on the Global Aerosol Data Set (GADS) (Koepke et al., 1997), compiled by d'Almeida et al. (1991) and described by Chin et al. (2000).

MOPSMAP used a different model for hygroscopicity, which is based on Zieger et al. (2013) and parameterized as

$$g(a_{\text{w}}) = \left(1 + \kappa \frac{a_{\text{w}}}{1 - a_{\text{w}}}\right)^{1/3}, \tag{32}$$

where $g(a_{\text{w}})$ is the hygroscopic growth factor (i.e., the ratio between the particle size at a specific relative humidity and particle size of a dry particle), a_{w} water activity, which can be replaced by relative humidity if the Kelvin effect can be neglected, and κ a measure of the particle's hygroscopicity when SPH particles with individual homogeneous composition are assumed (Zieger et al., 2013). For MOPSMAP, κ values were calculated from Figure 11 of Zieger et al. (2013). For BC, κ was set to 0.1.

Figure 1 shows the hygroscopic growth of GOCART aerosols modeled with CRTM and MOPSMAP. Hydroscopic aerosols increase with increasing relative humidity. A moderate linear increase is assumed for all aerosols below 80 %, the size of sea salt aerosols increases significantly at relative humidities larger than 95 %. Radii of dust,
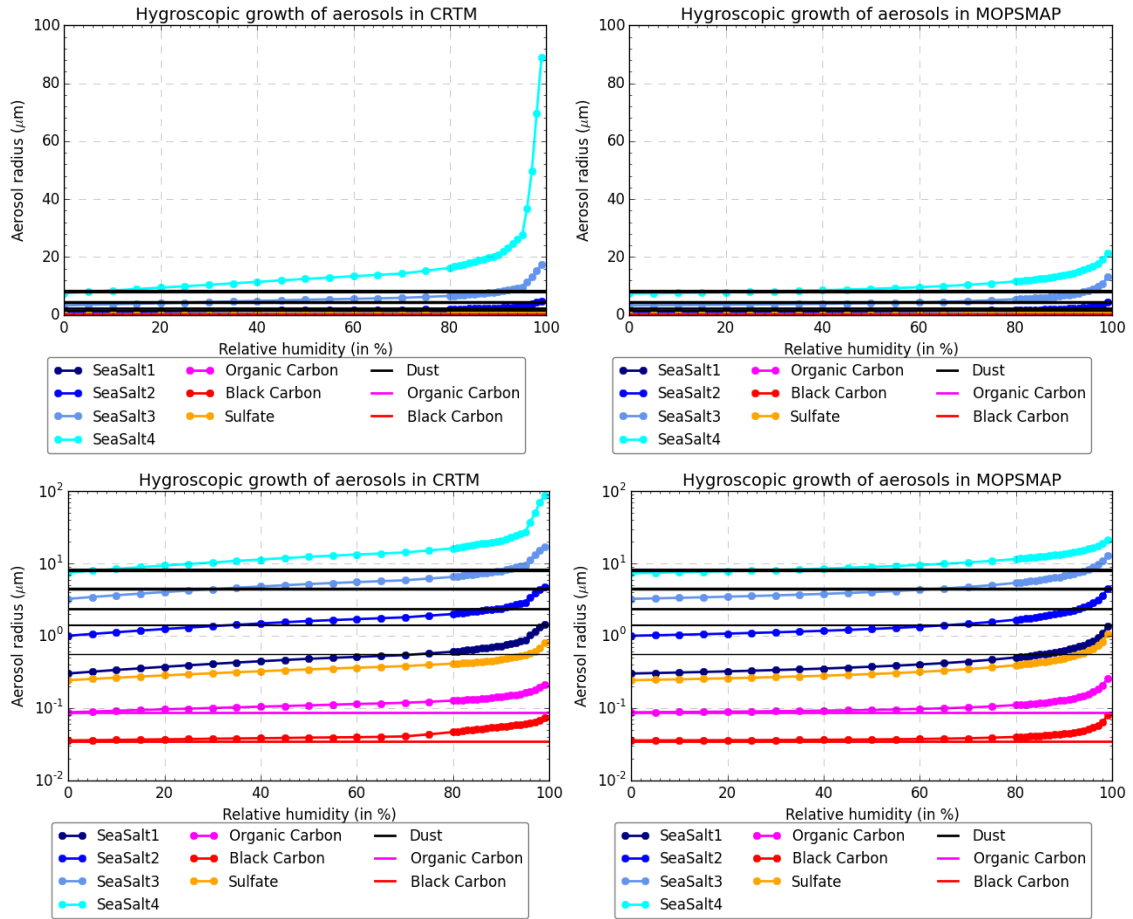
Figure 1: Hygroscopic growth of CRTM (left) and MOPSMAP (right) aerosols on a linear (top) and logarithmic (bottom) scale. Particles that do not grow with increasing humidity (such as dust, hydrophobic OC and BC) are additionally plotted with solid lines. Different line thicknesses of dust aerosols (black lines) indicate different dust particle sizes (thin to thick lines: 0.05 μm, 1.40 μm, 2.40 μm, 4.50 μm, 8.00 μm).

Table 1: GOCART aerosols types and their CRTM and MOPSMAP effective radii.

Aerosol type	CRTM r_{eff}(in μm)	MOPSMAP r_{eff}(in μm)
SPH dust	0.0098 to 7.9887	0.0098 to 7.8266
VEPS dust	—	0.0098 to 7.7625
CSEPS dust	—	0.0098 to 7.8262
Aerosols in SSAM	0.3001 to 1.4515	0.3000 to 1.3537
Aerosols in SSCM1	1.0001 to 4.8070	1.0000 to 4.4994
Aerosols in SSCM2	3.2500 to 17.2804	3.2479 to 13.0551
Aerosols in SSCM3	7.4951 to 88.8403	7.3576 to 21.2236
OC	0.0872 to 0.2122	0.0872 to 0.2572
BC	0.0355 to 0.0739	0.0355 to 0.0787
Sulfate	0.2424 to 0.7929	0.2424 to 1.0475

hydrophobic OC, and hydrophobic BC do not depend on relative humidity but are constant.

CRTM models a slightly larger hygroscopic growth than MOPSMAP. This is most evident for large relative humidities, where sea salt becomes as large as 89 μm in CRTM but only about 20 μm in MOPSMAP. At 50 % relative humidity, CRTM and MOPSMAP sea salt aerosols are as large as 12.43 μm and 8.98 μm, respectively (see Table 2).

3.3.2. Mass extinction coefficient

The mass extinction coefficient of aerosols (κ_{e} in m^2 kg^{-1}) depends on aerosol type, aerosol size, and measurement wavelength (CRTM and MOPSMAP contain information of 61 wavelengths from 200 nm to 37.037 μm). It is important to note that mass extinction coefficients of CRTM look-up tables are specified relative to dry aerosol mass. This means that all humidification effects are embodied in the value of the mass extinction efficiency (Chin et al., 2000).

Figure 2 shows the mass extinction coefficients as a function of wavelength at 10 % and 90 % relative humidity and as a function of aerosol size (including hygroscopic growth) at a wavelength of 550 nm for CRTM and MOPSMAP. Largest mass extinction coefficients are found for small wavelengths and small particles such as BC, OC, and sulfate. In the range of LIDAR wavelengths, small dust particles have larger mass extinction coefficients than large dust particles. This behavior changes for large measurement wavelengths. The comparison of mass extinction coefficients at 10 % and 90 % relative humidity reveals increasing κ_{e} with increasing relative humidity.

This is also shown at 550 nm, where mass extinction coefficients of all hygroscopic aerosols significantly increase with increasing size. Since aerosol size already includes hygroscopic growth, effective radii are proportional to the amount of ambient moisture.

Distinct differences between CRTM and MOPSMAP mass extinction coefficients are

Table 2: Characteristics of GOCART aerosols at 50 % relative humidity (no humidity influence on dust) and at a wavelength of 550 nm modeled with CRTM and MOPSMAP.

Aerosol type	r_{eff} (μm)	k_{e} (m^2 kg^{-1})	ω (1)	k_{b} (m^2 kg^{-1} sr^{-1})
		CRTM		
SPH dust	0.33	2181.0	0.99	42.24
VEPS dust	–	–	–	–
CSEPS dust	–	–	–	–
Aerosols in SSAM	0.48	7114.0	1.00	27.52
Aerosols in SSCM1	1.60	2164.0	1.00	57.47
Aerosols in SSCM2	5.21	587.3	1.00	38.33
Aerosols in SSCM3	12.43	262.0	1.00	20.65
OC	0.11	4578.0	0.98	38.17
BC	0.04	9918.0	0.20	47.23
Sulfate	0.34	7328.0	1.00	31.90
		MOPSMAP		
SPH dust	0.33	2173.4	0.96	81.48
VEPS dust	0.33	2211.4	0.96	45.30
CSEPS dust	0.33	2235.3	0.96	46.32
Aerosols in SSAM	0.37	4067.7	1.00	82.26
Aerosols in SSCM1	1.24	1350.5	1.00	63.19
Aerosols in SSCM2	4.03	358.8	1.00	31.48
Aerosols in SSCM3	8.98	154.3	1.00	19.88
OC	0.09	3014.5	0.97	64.72
BC	0.04	9248.1	0.20	91.80
Sulfate	0.30	5031.4	1.00	74.76
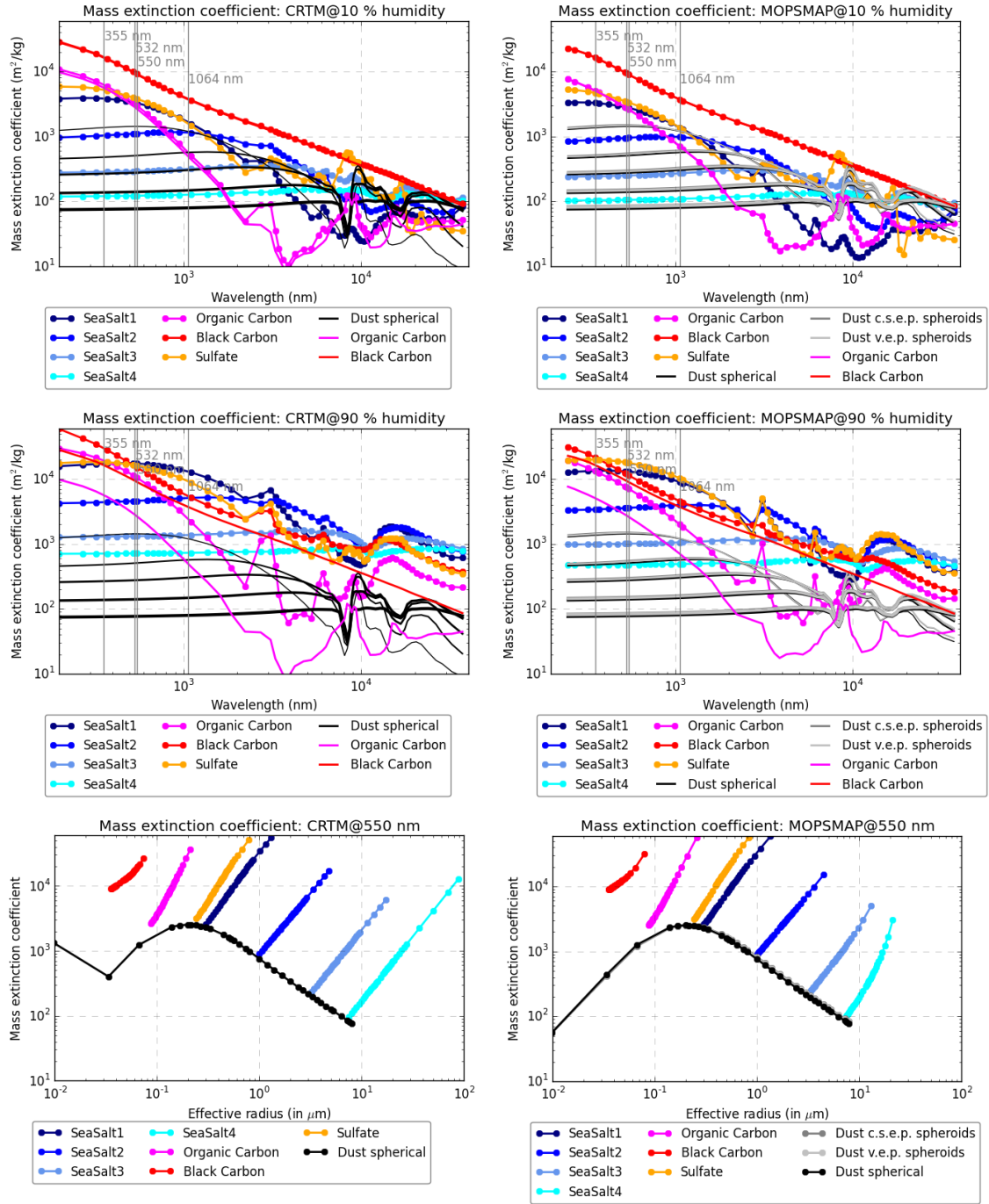
Figure 2: Mass extinction coefficients of CRTM (left) and MOPSMAP (right) as a function of wavelength at 10 % (top) and 90 % (middle) relative humidity and as a function of aerosol size at a wavelength of 550 nm (bottom). Particles that do not grow with increasing humidity (such as dust, hydrophobic OC and BC) are plotted with solid lines in the top and middle panels. Different line thicknesses of dust aerosols (black lines) indicate different dust particle sizes (thin to thick lines: 0.05 μm, 1.40 μm, 2.40 μm, 4.50 μm, 8.00 μm). The thin gray vertical lines in the top and middle panels indicate the three LIDAR wavelengths at 355 nm, 532 nm, and 1064 nm as well as the wavelength of many AOD measurements at 550 nm.

12

found for the smallest dust aerosol at a wavelength of 550 nm and at high relative humidities due to different modeling of ambient moisture effects. Table 2 summarizes these differences at a wavelength of 550 nm and 50 % relative humidity. It clearly shows that all CRTM mass extinction coefficients are larger than that of MOPSMAP. If the non-spherical shape of dust is accounted for, MOPSMAP mass extinction coefficients are slightly larger than that of spherical CRTM particles.

3.3.3. Single scatter albedo

The single scatter albedo for aerosol scatterers (w, dimensionless) depends on aerosol type, aerosol size, and measurement wavelength. Figure 3 shows the single scatter albedo as a function of wavelength at 10 % and 90 % relative humidity and as a function of aerosol size (including hygroscopic growth) at a wavelength of 550 nm for CRTM and MOPSMAP. Single scatter albedo ranges from zero to one. At small wavelengths, largest values are found for OC and sulfate. In the range of LIDAR wavelengths, small dust particles have larger single scatter albedo than larger dust particles, in general. This is not true for smallest dust aerosols as shown in the bottom panels of Figure 3. Single scatter albedo of non-spherical dust particles is slightly larger than that of spherical particles. The comparison of single scatter albedo at 10 % and 90 % relative humidity reveals increasing w with increasing ambient moisture.

Obvious differences between CRTM and MOPSMAP are again found for the smallest dust aerosol at a wavelength of 550 nm and for high relative humidities. Figure 3 and Table 2 show that most aerosols have single scatter albedo that is very close to one at a wavelength of 550 nm. Exceptions are BC (0.2 at 50 % relative humidity), OC (0.97/0.98 at 50 % relative humidity for MOPSMAP and CRTM, respectively), and dust. Dust particles with radii of 0.33 μm have a single scatter albedo of 0.96 in MOPSMAP and 0.98 in CRTM (see Table 2).

3.3.4. Mass backscattering coefficient

The CRTM mass backscattering coefficient κ_b (in $m^2\,kg^{-1}\,sr^{-1}$) was calculated offline (see above) and stored in the extended aerosol look-up table. Information of the corresponding MOPSMAP parameter was derived from the model itself (Gasteiger and Wiegner, 2018). Both aerosol look-up tables provide information of mass backscattering coefficients as a function of aerosol type, aerosol size, and measurement wavelength.

Figure 4 shows the mass backscattering coefficients of CRTM and MOPSMAP look-up tables as a function of wavelength at 10 % and 90 % relative humidity and as a function of aerosol size (including hygroscopic growth) at a wavelength of 550 nm. Largest backscattering coefficients are found for small wavelengths and for small aerosols such as OC, BC, and sulfate. The larger the size of the dust aerosols, the smaller the backscattering coefficients (with the exeption of very small dust particles as shown in the bottom panel of Figure 4). Smaller backscattering coefficients are also modeled for non-spherical dust particles. Higher amount of ambient moisture increases backscattering coefficients.

Problems occurred when reconstructing CRTM backscattering coefficients of some
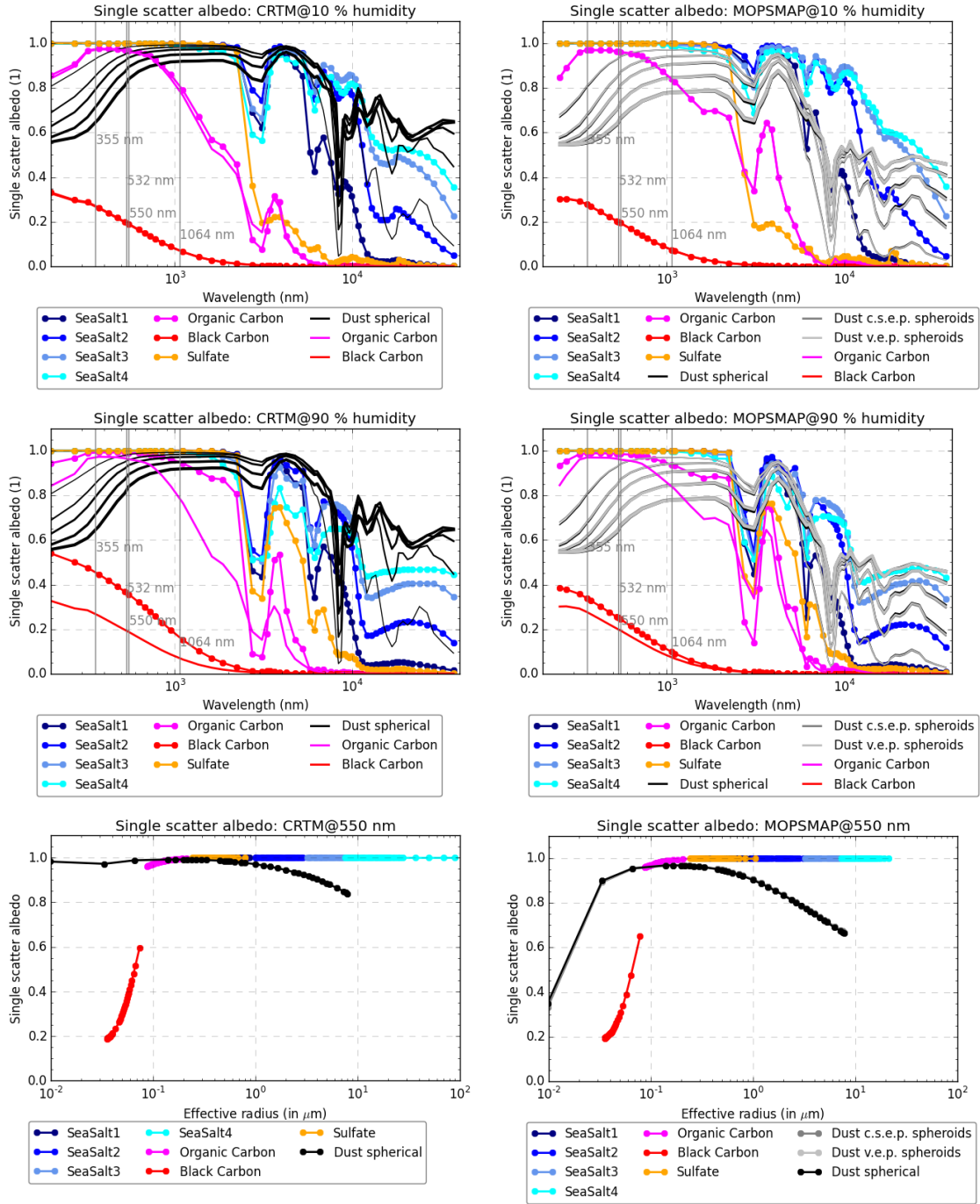
Figure 3: Single scatter albedo of CRTM (left) and MOPSMAP (right) as a function of wavelength at 10 % (top) and 90 % (middle) relative humidity and a function of aerosol size at a wavelength of 550 nm (bottom). Particles that do not grow with increasing humidity (such as dust, hydrophobic OC and BC) are plotted with solid lines in the top and middle panels. Different line thicknesses of dust aerosols (black lines) indicate different dust particle sizes (thin to thick lines: 0.05 μm, 1.40 μm, 2.40 μm, 4.50 μm, 8.00 μm). The thin gray vertical lines in the top and middle panels indicate the three LIDAR wavelengths at 355 nm, 532 nm, and 1064 nm as well as the wavelength of many AOD measurements at 550 nm.
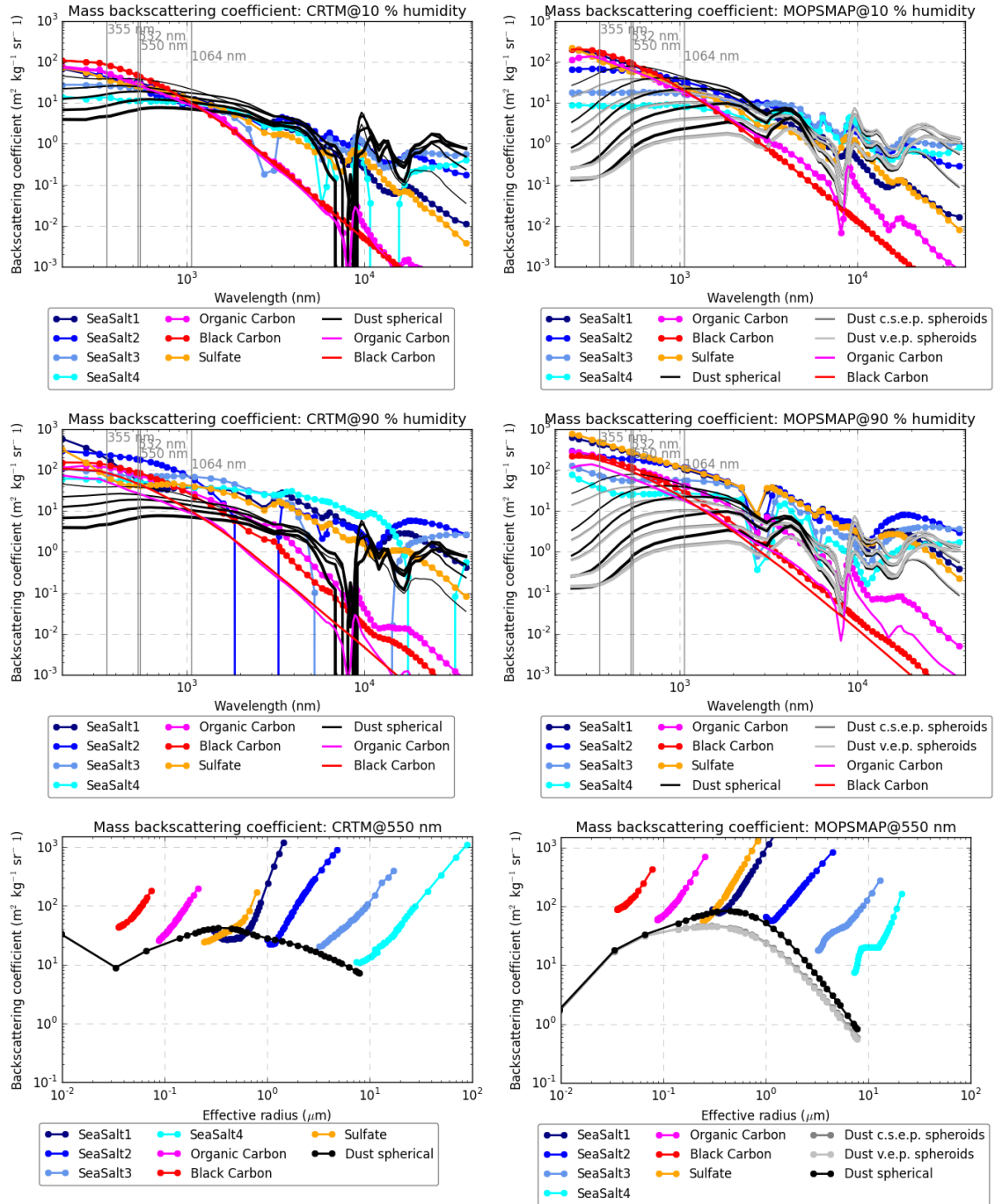
Figure 4: Mass backscattering coefficients of CRTM (left) and MOPSMAP (right) as a function of wavelength at 10 % (top) and 90 % (middle) relative humidity and as a function of aerosol size at a wavelength of 550 nm (bottom). Particles that do not grow with increasing humidity (such as dust, hydrophobic OC and BC) are plotted with solid lines in the top and middle panels. Different line thicknesses of dust aerosols (black lines) indicate different dust particle sizes (thin to thick lines: 0.05 μm, 1.40 μm, 2.40 μm, 4.50 μm, 8.00 μm). The thin gray vertical lines in the top and middle panels indicate the three LIDAR wavelengths at 355 nm, 532 nm, and 1064 nm as well as the wavelength of many AOD measurements at 550 nm.

aerosol types at some wavelengths. Even negative coefficients were reconstructed. Figure 4 shows these features, e.g., for CRTM backscattering coefficients of sea salt 2 at 90 % relative humidity between about 2000 nm and 3000 nm (in the infrared part of the spectrum). A potential reason of this behavior is a deficiency of the phase coefficients of the original CRTM aerosol look-up table. Since this problem did not affect backscattering coefficients at LIDAR wavelengths, data were still used for further calculations.

Dinstinct differences between CRTM and MOPSMAP mass backscattering coefficients are found for dust, where CRTM coefficients are larger than that of MOPSMAP at small wavelengths. At a wavelength of 550 nm, MOPSMAP medium-size dust aerosols have larger backscattering coefficients than corresponding CRTM aerosols.

Backscattering coefficients of other GOCART aerosols are also modeled differently but these differences are more complex than for other optical properties. At a wavelength of 550 nm and 50 % relative humidity, e.g., small sea salt aerosols (SSAM and SSCM1) have larger backscattering coefficients in MOPSMAP but SSCM2 and SSCM3 aerosols have larger coefficients in CRTM (see Table 2).

The evaluation of CRTM runs with different parameter settings will reveal adequacies and deficiencies of CRTM and MOPSMAP model parameterizations, discussed in the next section.

4. CRTM evaluation

4.1. Input data

Information about aerosol concentrations and AOP have been made available by NASA. The MERRA Aerosol Reanalysis (MERRAero) is based on the Goddard Earth Observing System Data Assimilation System version 5 (GEOS-5) model driven by Modern Era Retrospective-analysis for Research and Applications (MERRA) meteorological reanalyses. These data cover the period from January 2002 to February 2016. The production of MERRAero (MERRA-1) data has been discontinued end of February 2016 because of the availability of MERRA-2 data. The new MERRA-2 data are available from 1980 to present. The spatial resolution of both data sets is 0.625° in longitude, 0.5° in latitude, at 72 vertical eta levels. Global gridded fields are therefore available on 576 grid points in longitude, 361 grid points in latitude, and 72 grid points with height (hybrid-eta levels from the surface to 0.01 hPa).

Both MERRA data sets provide global fields of the concentration of dust, sea salt, sulfate, black and organic carbon. One MERRA-1[1] and one MERRA-2[2] file from 17 April 2010, 12 UTC were used as input to calculate AOP with CRTM.

In addition to aerosol concentrations, MERRA-1 and MERRA-2 also provide information about AOD at 550 nm. These data were used to validate AOD calculated with CRTM. Furthermore, MERRA-1 provides information about aerosol extinction and backscattering coefficients at three different wavelengths (355 nm, 532 nm and 1064 nm) as observed by LIDAR measurements. Because corresponding MERRA-2 data are not publicly available, only MERRA-1 data were used to validate lidar-based AOP from CRTM.

The following links give further information about MERRA:

- MERRA-1 data download:

  `https://gmao.gsfc.nasa.gov/reanalysis/merra/MERRAero/data/`

- MERRA-1 documentation:

  `https://gmao.gsfc.nasa.gov/reanalysis/merra/MERRAero/docs/`

- MERRA-2 data download:

  `https://disc.sci.gsfc.nasa.gov/daac-bin/FTPSubset2.pl`

- MERRA-2 data documentation:

  `https://gmao.gsfc.nasa.gov/reanalysis/MERRA-2/docs/`

  `https://gmao.gsfc.nasa.gov/pubs/docs/Randles887.pdf`

---

[1] MERRA-1 file: `dR_MERRA-AA-r2.inst3hr_3d_aer_Nv.20100417_1200z.nc4`
[2] MERRA-2 file: `MERRA2_300.inst3_3d_aer_Nv.20100417.SUB.nc4`

4.2. CRTM model runs

Several CRTM model configurations were tested and validated:

CRTM(SPH, MERRA-1): CRTM calculations were done with MERRA-1 aerosol concentrations and the extended CRTM aerosol look-up table. This table contains information of SPH particles only.

CRTM(SPH, LR, MERRA-1): CRTM calculations were done with MERRA-1 aerosol concentrations and the extended CRTM aerosol look-up table. This table contains information of SPH particles only. Backscattering coefficients were calculated by assuming a constant LIDAR ratio.

CRTM(SPH, MERRA-2): CRTM calculations were done with MERRA-2 aerosol concentrations and the extended CRTM aerosol look-up table. This table contains information of SPH particles only.

CRTM(SPH, LR, MERRA-2): CRTM calculations were done with MERRA-2 aerosol concentrations and the extended CRTM aerosol look-up table. This table contains information of SPH particles only. Backscattering coefficients were calculated by assuming a constant LIDAR ratio.

MOPSMAP(SPH, MERRA-1): CRTM calculations were done with MERRA-1 aerosol concentrations and the MOPSMAP aerosol look-up table. Only SPH particles were used.

MOPSMAP(SPH, LR, MERRA-1): CRTM calculations were done with MERRA-1 aerosol concentrations and the MOPSMAP aerosol look-up table. Only SPH particles were used. Backscattering coefficients were calculated by assuming a constant LIDAR ratio.

MOPSMAP(VEPS, MERRA-1): CRTM calculations were done with MERRA-1 aerosol concentrations and the MOPSMAP aerosol look-up table. VEPS particles were used to simulate AOP of dust.

MOPSMAP(CSEPS, MERRA-1): CRTM calculations were done with MERRA-1 aerosol concentrations and the MOPSMAP aerosol look-up table. CSEPS particles were used to simulate AOP of dust.

MOPSMAP(SPH, MERRA-2): CRTM calculations were done with MERRA-2 aerosol concentrations and the MOPSMAP aerosol look-up table. Only SPH particles were used.

MOPSMAP(SPH, LR, MERRA-2): CRTM calculations were done with MERRA-2 aerosol concentrations and the MOPSMAP aerosol look-up table. Only SPH particles were used. Backscattering coefficients were calculated by assuming a constant LIDAR ratio.

MOPSMAP(VEPS, MERRA-2): CRTM calculations were done with MERRA-2 aerosol concentrations and the MOPSMAP aerosol look-up table. VEPS particles were used to simulate AOP of dust.

MOPSMAP(CSEPS, MERRA-2): CRTM calculations were done with MERRA-2 aerosol concentrations and the MOPSMAP aerosol look-up table. CSEPS particles were used to simulate AOP of dust.

4.3. Evaluation of AOD

Aerosol concentrations of the MERRA-1 and MERRA-2 reanalyses were used to compute total AOD at 550 nm as measured by the MODIS instrument onboard the Aqua and Terra satellites. Since CRTM output is a vertical profile of the dimensionless aerosol optical depth (see Eq. 1), it has to be vertically integrated

$$\text{AOD}' = \sum_{n=1}^{\text{n\_layers}} \text{AOD}(n). \tag{33}$$

4.3.1. Model-to-model comparison

Figure 5 shows AOD from MERRA-2, CRTM(SPH, MERRA-2), and MOPSMAP(SPH, MERRA-2). Highest aerosol loads are found above the Saharan region in North Africa as well as in East Asia. High AOD in the northwestern part of Russia might be caused by aerosols from the volcanic eruption of the Eyjafjallajökull in April 2010.

The comparison between the models visualizes different model parameterizations and model assumptions because input aerosol concentrations were identical for all runs. This comparison reveals higher AOD in CRTM and MOPSMAP over the oceans (slightly smaller differences for MOPSMAP than for CRTM) but smaller AOD over continental regions with high dust load (such as over the Saharan region in Africa).

To further investigate the impact of the aerosol shape on AOD, Figure 6 shows the AOD differences for spheriods (CSEPS and VEPS) and spherical particles calculated with MOPSMAP. Positive differences indicate larger aerosol extinction for spheroids than for spherical particles. This is consistent with larger mass extinction coefficients of non-sperical than of spherical particles as shown in Figure 2 and Table 2.

Since MOPSMAP models spheroids only for dust aerosols, AOD differences are largest over dusty regions, where they are, in general, smaller than 0.1. This is too small to change the general picture of the MOPSMAP versus MERRA-2 comparison shown in Figure 5. This means that above the Saharan region in North Africa and in East Asia, AOD from prolate spheroids from MOPSMAP is still smaller than that of MERRA-2.

4.3.2. Comparison to observations

The AErosol RObotic NETwork (AERONET) is a global ground-based aerosol monitoring network that uses automatic sun-sky scanning spectral radiometers. Level 2 of these
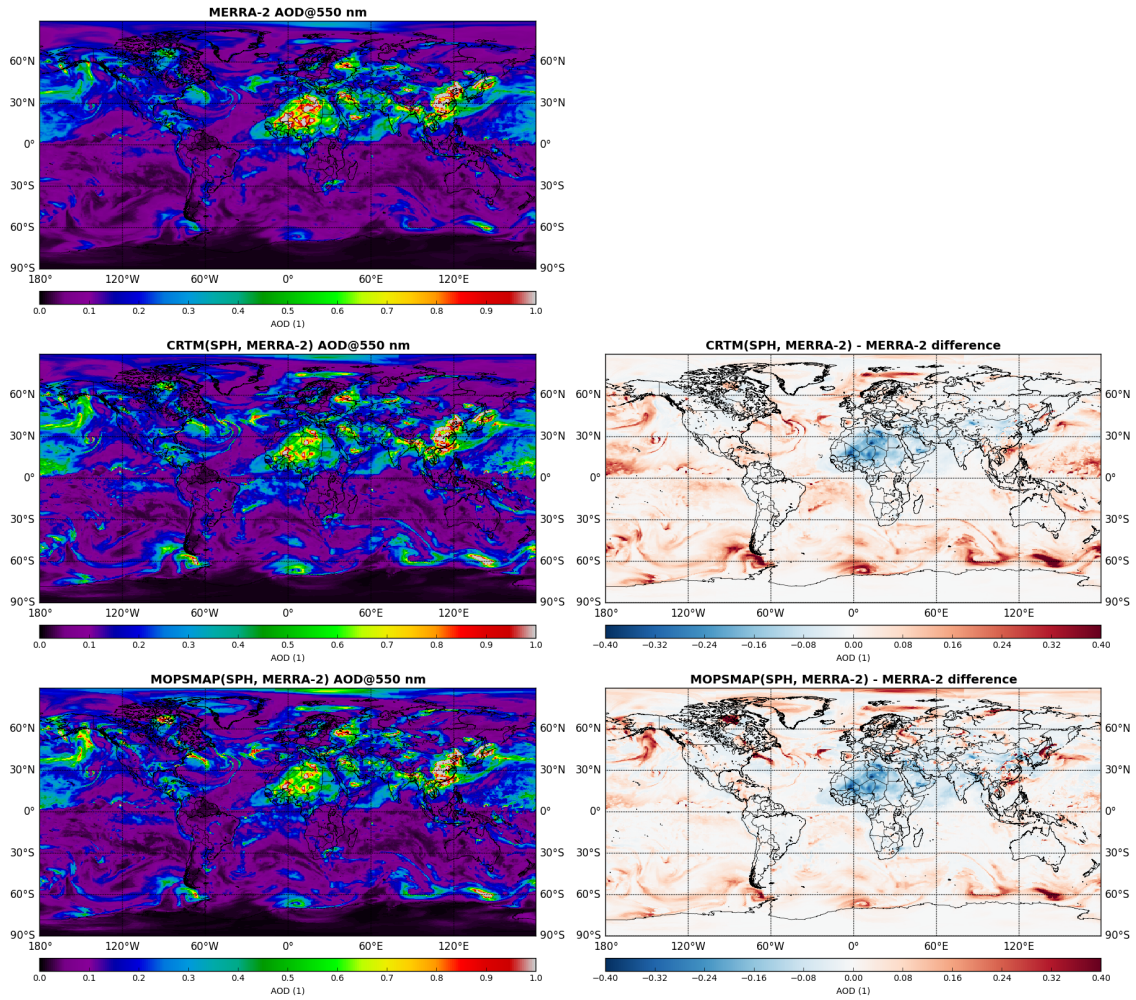
Figure 5: AOD at 550 nm (left) from MERRA-2 (top), CRTM(SPH, MERRA-2) (middle), and MOPSMAP(SPH, MERRA-2) (bottom) and their differences relative to MERRA-2 (right).
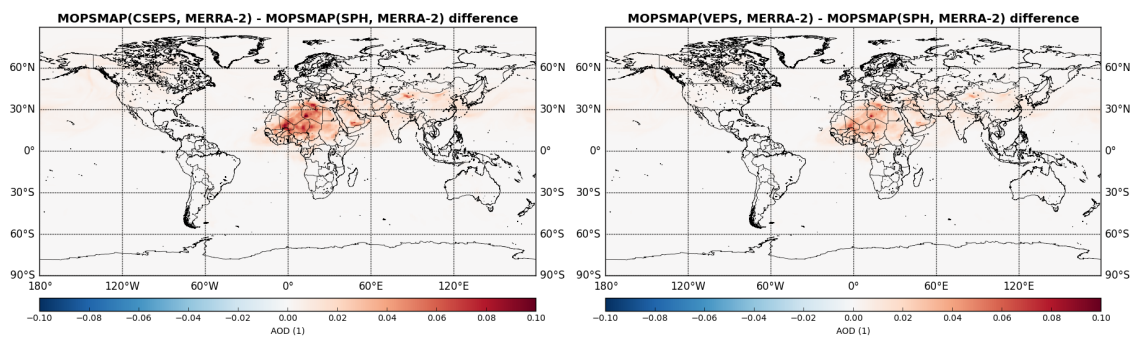
Figure 6: AOD difference at 550 nm from MOPSMAP(CSEPS, MERRA-2) (left) and MOPSMAP(VEPS, MERRA-2) (right) relative to MOPSMAP(SPH, MERRA-2). Note the different colorbar compared to Figure 5.
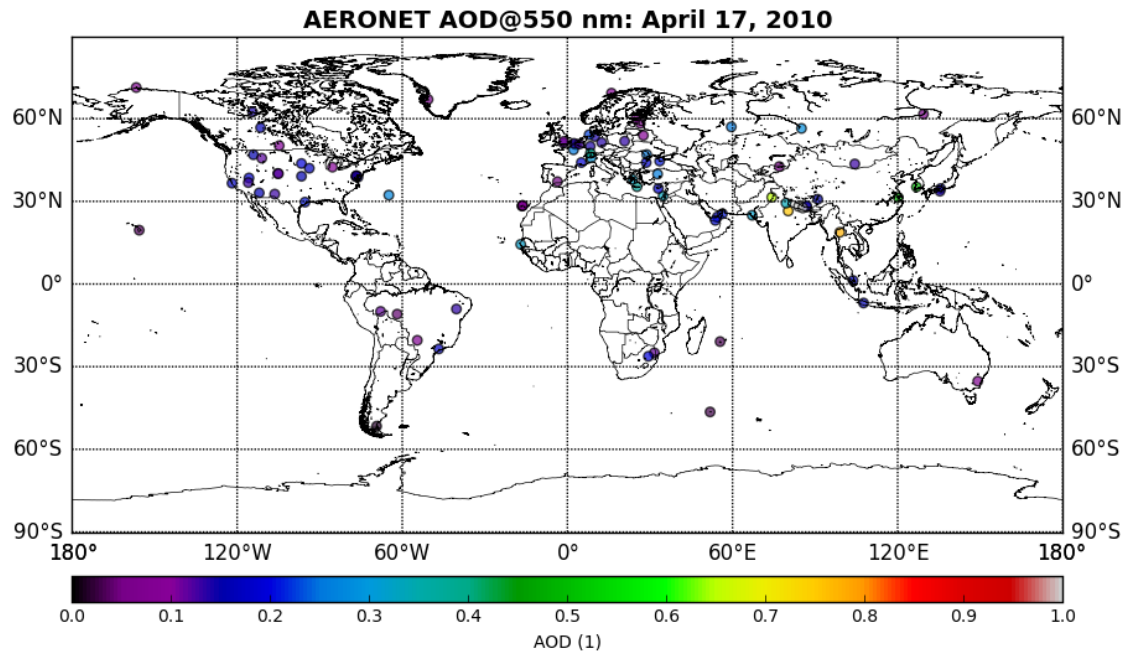
Figure 7: Daily mean AOD at 550 nm observed with AERONET on 17 April 2010.

data were used to validate modeled AOD. To compare the data at the same wavelength, AERONET AOD was interpolated to 550 nm using measured AOD at 500 nm and the Ångström coefficient α from 440 nm and 675 nm

$$\mathrm{AOD}_{550} = \mathrm{AOD}_{500} \left(\frac{550}{500} \right)^{-\alpha}. \tag{34}$$

Figure 7 shows daily mean AERONET AOD observations on 17 April 2010. Most of the 91 measurement sites were located over the continental U.S. and in Europe. Only a few measurements were made available in South America, Africa, Asia, and Australia. Highest AOD values were observed in India, Nepal, and south-east Asia. Two measurement sites even observed daily-mean AOD values larger than one. These were the stations in Pokhara, Nepal (83.98° longitude, 28.19° latitude) and Kathmandu, Nepal (85.54° longitude, 27.60° latitude).

Scatter plots of observed and modeled AOD are shown in Figure 8 (the left panel shows results for MERRA-1, the right panel for MERRA-2). In general, all models are in good agreement with the observations with a small positive model bias for small AOD (< 0.35) and a small negative model bias for high AOD (> 0.6). A potential reason for these consistent model biases is a small bias of MERRA aerosol concentrations that were used as input for all computations. Furthermore, results might be affected by the representativeness error, caused by the comparison of daily-mean observed AOD and AOD simulated for 12 UTC.

All model runs have very similar performance when MERRA-1 input data were used. Worse model consistency is found for MERRA-2 input data. Besides that, MERRA-1

21
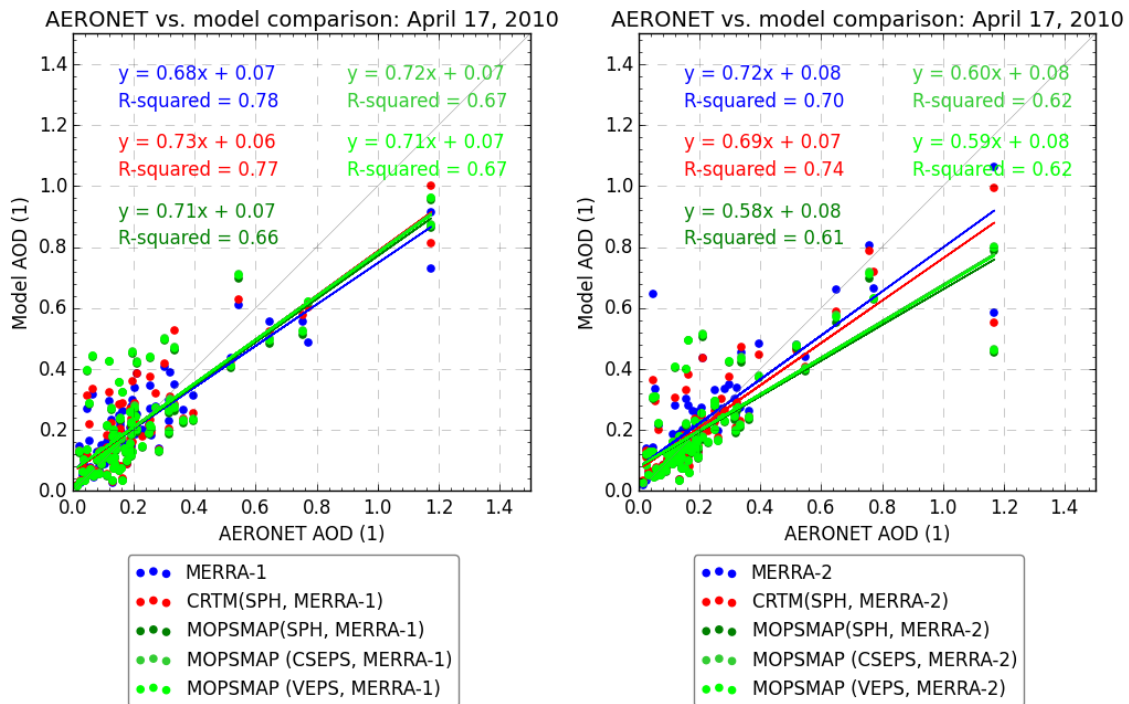
Figure 8: Scatter plot of daily mean AOD measurements from the AERONET and AOD from different aerosol models. The left scatter plot shows results of MERRA-1 input data, the right scatter plot those of MERRA-2 input data.

model runs have higher r^2 values than MERRA-2 runs.

Different performance of CRTM and MOPSMAP from MERRA-1 and MERRA-2 indicates different aerosol composition of MERRA-1 and MERRA-2 data because the same models, same parameterizations but different aerosol fields were used as input. Furthermore, it seems that optical properties changed (improved) between these two MERRA data versions. To better understand these differences, however, a more detailed investigation is needed. This investigation should also include looking at the aerosol composition at specific measurement sites, but it is out of the scope of this study.

4.4. Evaluation of LIDAR optical properties

Aerosol concentrations of the MERRA-1 and MERRA-2 reanalyses were also used to compute AOP as observed by LIDAR instruments. Since CRTM operates on height/thickness independent quantities, volume extinction and backscattering coefficients are dimensionless and have to be re-scaled to obtain appropriate units:

$$E'(z) = \frac{E(z)}{\mathrm{d}z} \tag{35}$$

and

$$B'(z) = \frac{B(z)}{\mathrm{d}z} \tag{36}$$

with $\mathrm{d}z$ (in m) being the layer depth, which can be obtained from

$$\mathrm{d}z = -\frac{\mathrm{d}p(z)}{g\varrho(z)}, \tag{37}$$

when using MERRA data (see also Section C.3).

4.4.1. Model-to-model comparison

Figure 9 shows aerosol extinction and backscattering coefficients as well as the LR at 532 nm from the MERRA-1 reanalysis on 17 April 2010, 12 UTC. Larger aerosol concentrations in the lower atmosphere cause increasing extinction and backscattering coefficients towards the surface. The median extinction coefficient increases from approximately 5×10^{-4} km^{-1} at 100 hPa to 2×10^{-2} km^{-1} at 900 hPa. Similarly, the median backscattering coefficient increases from approximately 7×10^{-6} km^{-1}sr^{-1} at 100 hPa to 5×10^{-4} km^{-1}sr^{-1} at 900 hPa. The slightly larger increase of backscattering coefficients yields decreasing LR towards the surface. The median LR profile decreases from 70 sr^{-1} at 100 hPa to 40 sr^{-1} at 900 hPa.

Individual profiles reveal that global extinction and backscattering coefficients can vary more than two orders of magnitude. This is reasonable and can be attributed to aerosol-loaded and clear-air conditions.

It is also important to note that we found some MERRA-1 data quality issues with aerosol concentrations being exactly zero at some pressure levels. These missing data were filled with log-linear interpolation. Large differences between mean and median
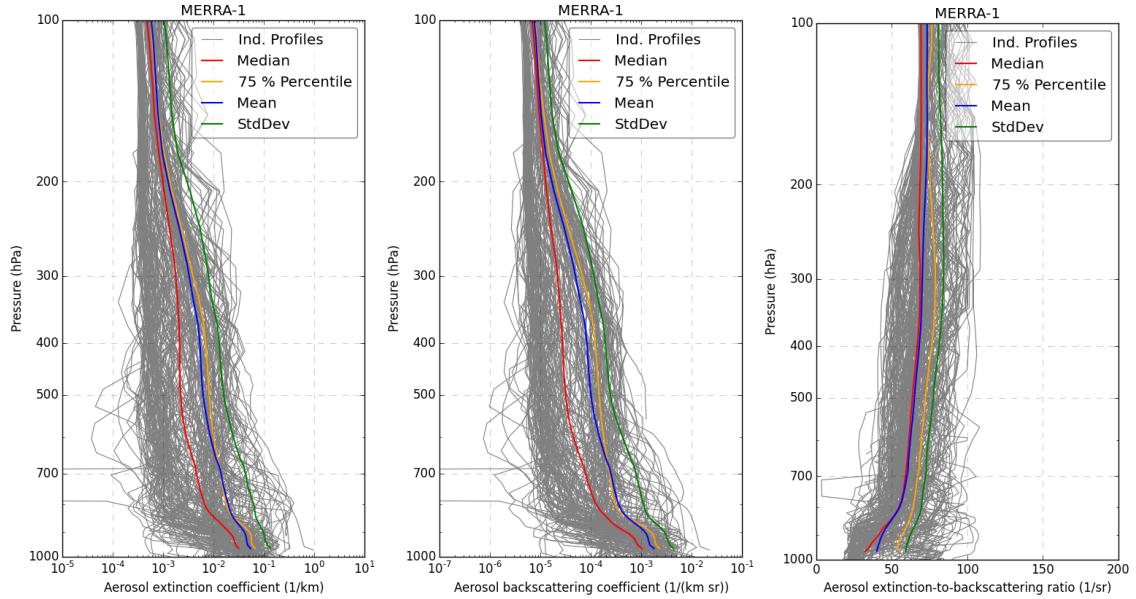
Figure 9: Vertical profiles of MERRA-1 AOP: aerosol extinction coefficients (left), backscattering coefficients (middle), and extinction-to-backscattering ratio (right). Results are shown for the visible part of the spectrum. Individual profiles are shown in gray (out of 207936 profiles, only every 1000th profile is plotted), median in red, the 75 % percentile in yellow, the mean in blue, the standard deviation in green.

profiles as well as large standard deviations also indicate a large number of outlier profiles. Unfortunately, MERRA-2-derived AOP from LIDAR measurements are not yet publicly available and cannot be used for validation.

Figure 10 shows the differences of aerosol extinction and backscattering coefficients of CRTM(SPH, MERRA-1) and MOPSMAP(SPH, MERRA-1) relative to MERRA-1. Backscattering coefficients were obtained from both methods (i) the aerosol look-up tables and (ii) by assuming a constant LR for individual aerosol types (Eq. 12). Note that CRTM and MOPSMAP results are obtained at 550 nm and not at 532 nm as the MERRA-1 reference. However, results are not expected to vary much between these wavelengths (see Figs. 2 and 4).

In general, CRTM, MOPSMAP, and MERRA-1 extinction coefficients are in good agreement. Median CRTM differences are within ±25 % with negative differences (i.e., smaller CRTM extinction coefficients) at altitudes above about 850 hPa and positive differences below. Median MOPSMAP extinction coefficients are also within 25 % but they are systematically negative in the entire troposphere.

Median systematic difference of the backscattering coefficients calculated with the CRTM look-up table decreases from −50 % at 100 hPa to −25 % at 700 hPa. In the atmospheric boundary layer, CRTM backscattering coefficients are larger than that of MERRA-1 and differences become positive. In contrast, MOPSMAP backscattering coefficients are larger than that of MERRA-1 in the entire troposphere. Assuming a constant LR, the differences between the models are smaller. Median differences between
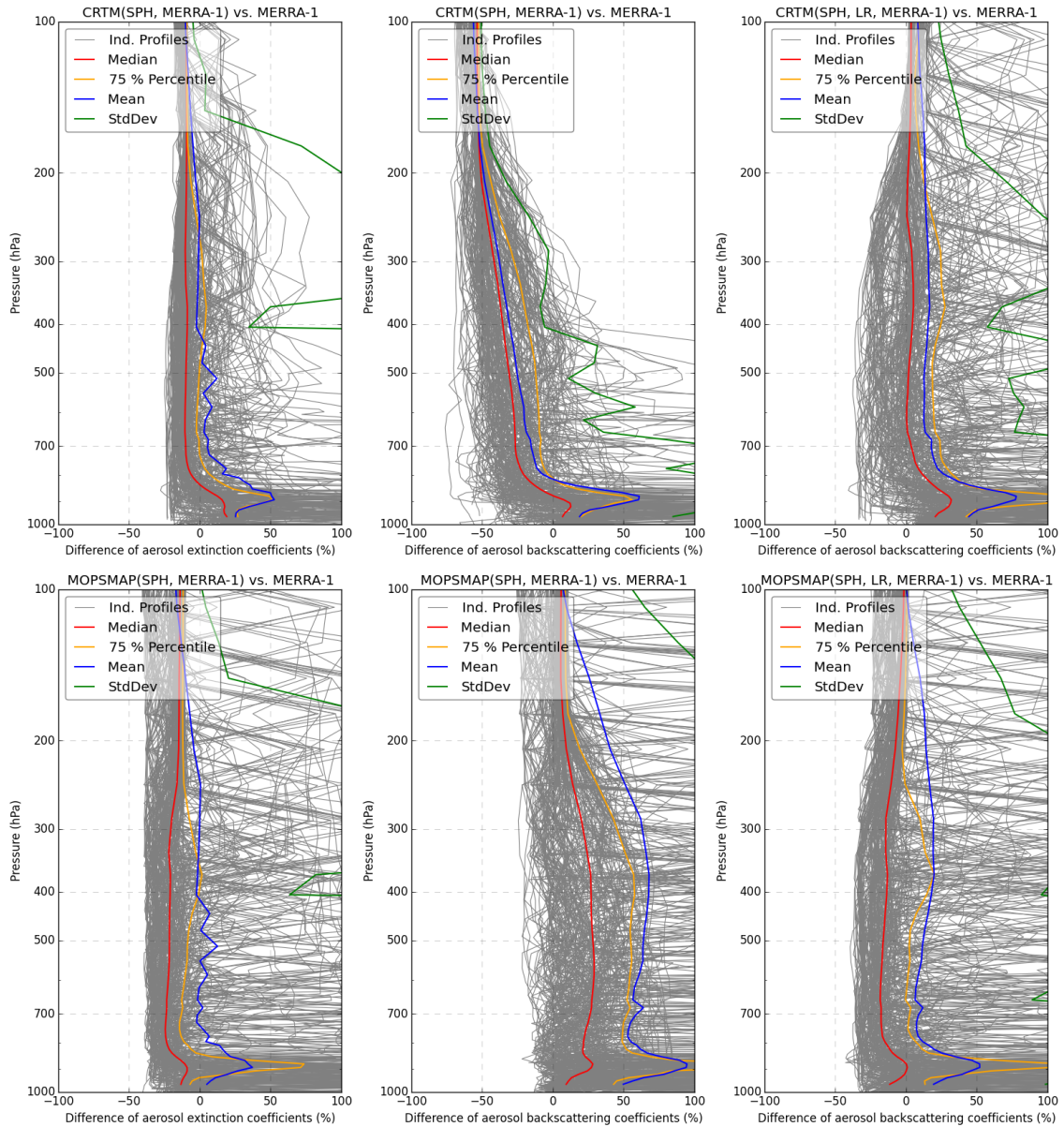
Figure 10: Vertical difference profiles of aerosol extinction coefficients (left), aerosol backscattering coefficients (middle), and aerosol backscattering coefficients from a fixed LR (right) of CRTM (top) and MOPSMAP (bottom) relative to MERRA-1. CRTM and MOPSMAP both used MERRA-1 aerosol concentrations and assumed spherical particles only. Results are shown for the visible part of the spectrum.
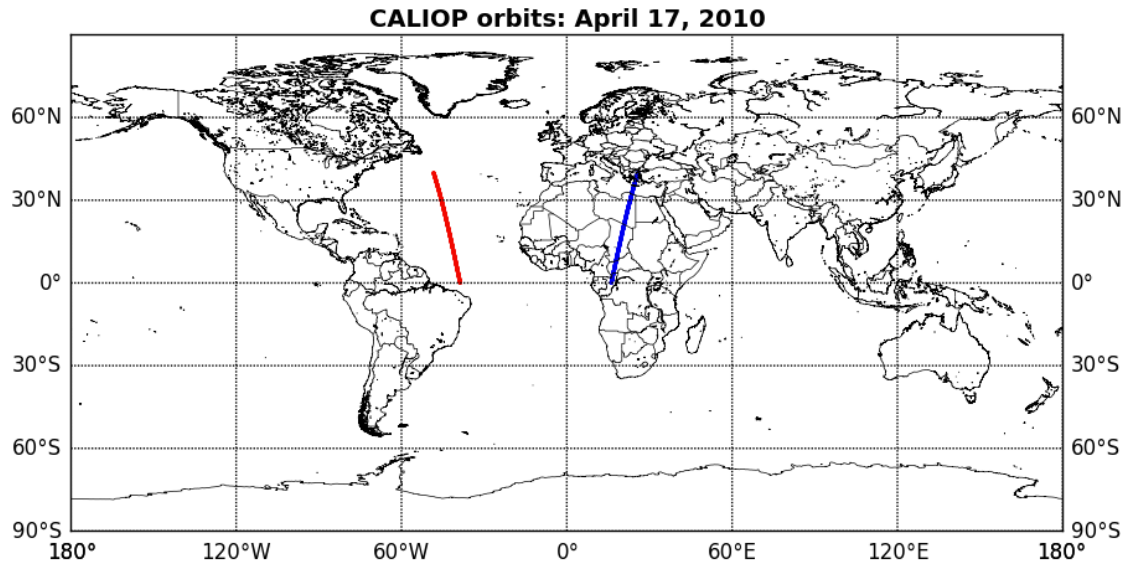
Figure 11: CALIOP orbit segments used for evaluation. Day-time measurements are shown in red, night-time measurements in blue.

CRTM and MERRA-1 are smaller than 5 % in large parts of the atmosphere. Those of MOPSMAP are again mainly negative but remain within approximately -15 %.

Individual extinction and backscattering coefficient difference profiles have a lot of spikes larger than 100 %, yielding also a large difference between the median and the mean as well as a large standard devitation. A first closer look at these differences showed that they are related to atmospheric humidity and different modeling of ambient moisture effects (see Section 3.3).

4.4.2. Comparison to observations

The Cloud-Aerosol Lidar with Orthogonal Polarisation (CALIOP) instrument onboard the Cloud-Aerosol Lidar and Infrared Pathfinder Satellite Observations (CALIPSO) satellite measures aerosol and cloud characteristics with a LIDAR technique at two wavelengths at 532 nm and 1064 nm. Retrieved backscattering and extinction coefficients are provided, e.g., by NASA.

To validate the quality of vertically-resolved modeled AOP, we selected a set of CALIOP measurements over North Africa[3] and the North Atlantic[4]. The locations of these two orbit segments are shown in Figure 11. Measurements above Africa were obtained from approximately 0:30 UTC to 0:41 UTC, those above the North Atlantic were performed from approximately 16:21 UTC to 16:32 UTC. Even though these measurements are not co-located in time with the model simulations, we choose these two orbit segments to better understand the impact of dust and sea salt on modeled AOP.

---

[3]CALIOP file: `CAL_LID_L2_05kmAPro-Standard-V4-10.2010-04-17T00-22-35ZN_Subset.hdf`

[4]CALIOP file: `CAL_LID_L2_05kmAPro-Standard-V4-10.2010-04-17T15-59-02ZD_Subset.hdf`
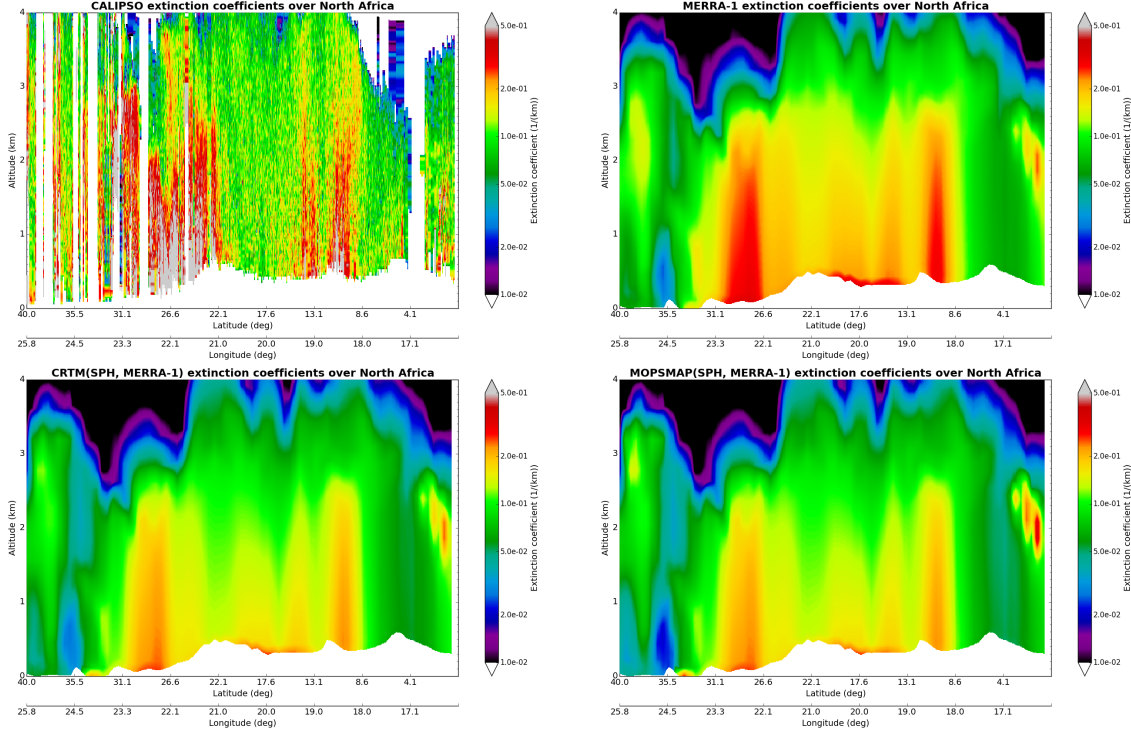
Figure 12: Vertically-resolved extinction coefficients from CALIPSO measurements on 17 April 2010 over North Africa (top left) and model results from MERRA-1, CRTM(SPH, MERRA-1), and MOPSMAP(SPH, MERRA-1).

CALIOP variables names were `Extinction_Coefficient_532` for extinction coefficients and `Total_Backscatter_Coefficient_532` for backscattering coefficients.

Figures 12, 13, 14, and 15 show validation results for the overpass over Africa, Figures 16, 17, 18, and 19 show results over the North Atlantic. To make a meaningful comparison, model data were horizontally interpolated to CALIOP observation locations. Furthermore, all data were vertically interpolated to a common pressure grid, defined as $p = p_{surf} \exp(-z/H)$ with $p_{surf} = 101325$ Pa being surface pressure, z being an equidistant altitude grid from the surface to 5 km, and $H = 7000$ m being the atmospheric scale height.

Figure 12 reveals largest CALIOP extinction coefficients between about 10°N and 14°N as well as between 22°N and 32°N. MERRA-1 captured best the magnitude of these measurements even though they were slightly smaller than the observed values. CRTM and MOPSMAP extinction coefficients were clearly too low in this region. Better agreement between CRTM/MOPSMAP and CALIOP was found between 14°N and 22°N, where MERRA-1 overestimated aerosol extinction.

Figure 13 shows mean profiles of model minus observation extinction coefficient differences for MERRA-1 and MERRA-2 input data. Differences were only calculated where CALIOP measurements were available. MERRA-1 data are in best agreement with CALIOP observations. All CRTM/MOPSMAP simulations consistently show a nega-

27
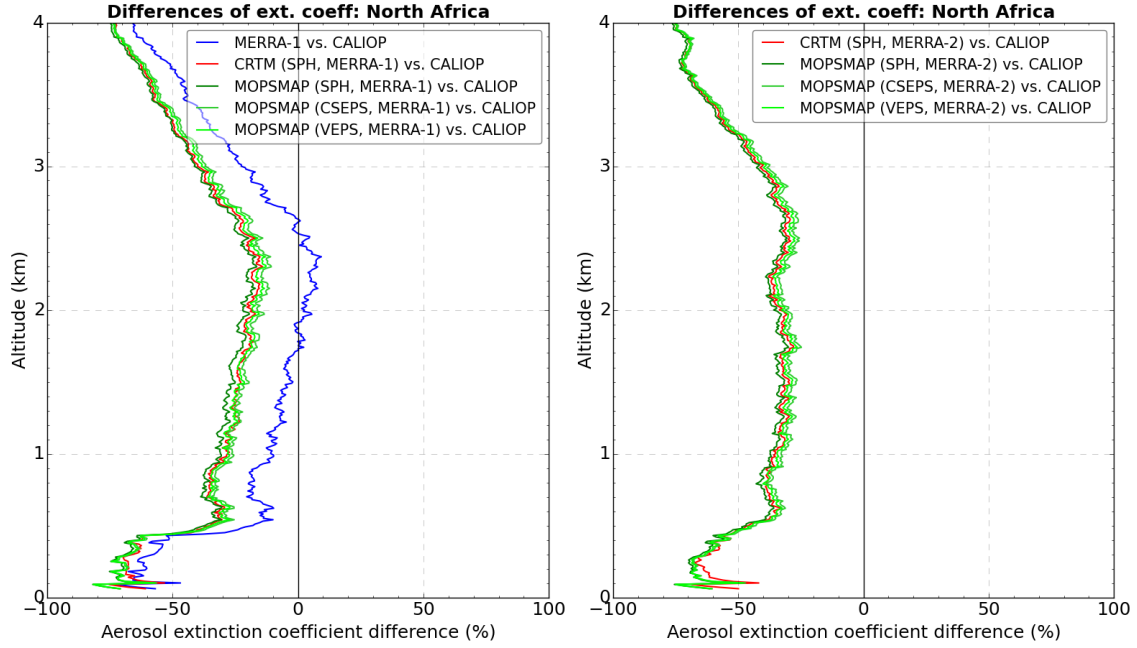
Figure 13: Model minus observation extinction coefficient difference profiles over Africa from different model simulations. Results are shown for MERRA-1 (left) and MERRA-2 (right) input data.

tive bias (i.e., modeled extinction coefficients are too low). The bias is larger than 50 % in the atmospheric boundary layer, becomes smaller than 30 % at 2 km, and increases again above about 2.5 km.

Figure 14 shows backscattering coefficients of the CALIOP overpass over Africa. The spatial pattern is very similar to that of extinction coefficients with largest backscattering found between about 10°N and 14°N and between 22°N and 32°N. MERRA-1 again captures this pattern and its magnitude reasonably well. While backscattering coefficients of spherical particles from the CRTM and MOPSMAP aerosol look-up tables are too large, they are too small if a constant LIDAR ratio is assumed. Distinctively better results are found when using non-spherical dust particles provided by MOPSMAP.

These results are also shown in mean backscattering coefficient difference profiles (Figure 15). The mean MOPSMAP(SPH, MERRA-1) bias is largest, it almost reaches 100 % slightly above 2 km. At the same level, the CRTM(SPH, MERRA-1) bias is about 50 %. The bias of mean backscattering coefficients obtained with a constant LR is consistently negative and amounts approximately to −30 % to −50 % above the atmospheric boundary layer up to an altitude of 3 km. MERRA-1 and simulations with non-spherical dust particles closest match the observations with biases being, in general, within −30 % above the atmospheric boundary layer up to 3 km.

Above the North Atlantic, aerosol extinction coefficients are distinctively smaller than over Africa (cp. Figs. 12 and 16 but note different range of y-axes). CALIOP extinction coefficients rarely exceed 3 km^{-1} over the North Atlantic. While MERRA-1 clearly underestimates extinction of sea salt aerosols, CRTM(SPH, MERRA-1) and
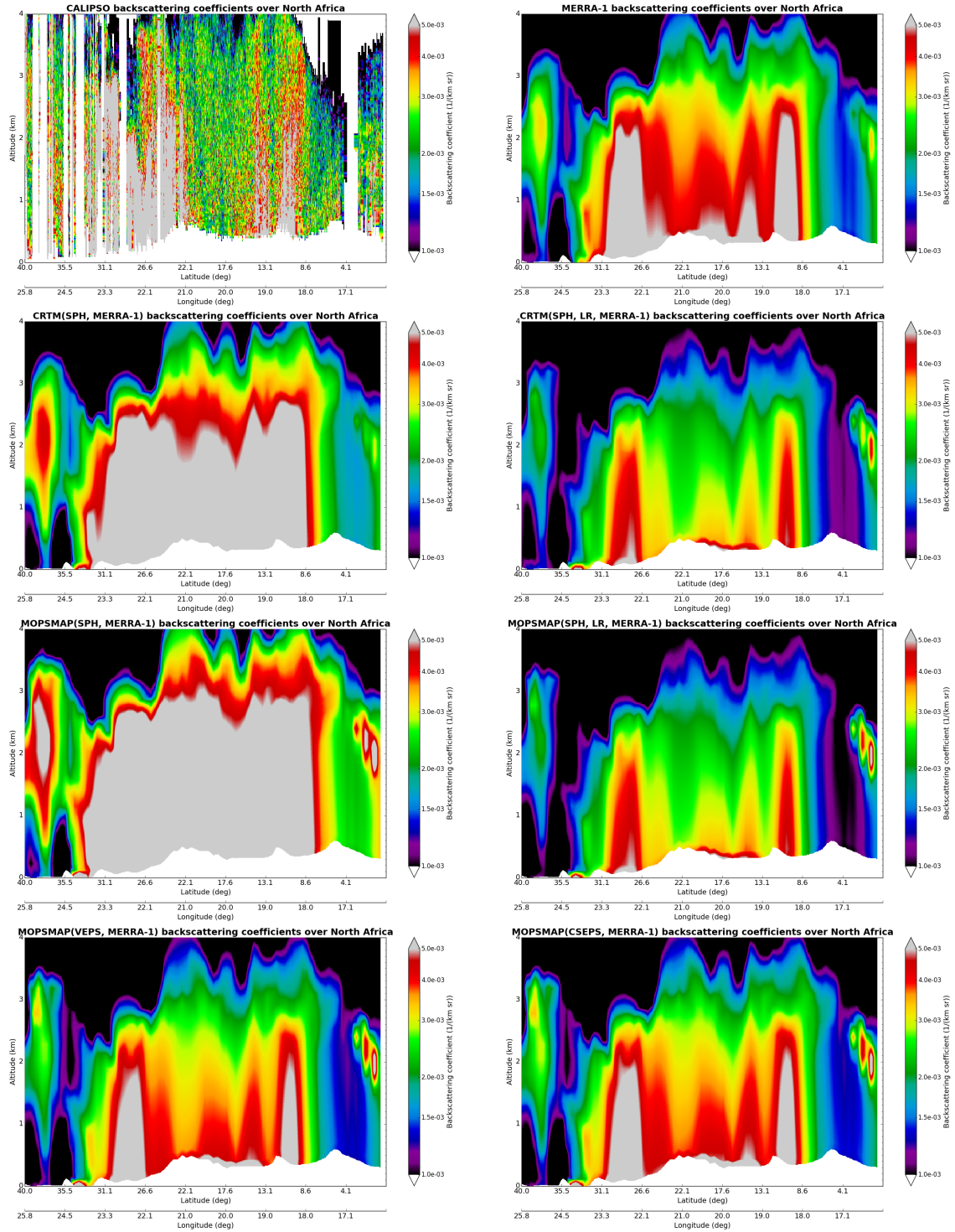
Figure 14: Vertically-resolved backscattering coefficients from CALIPSO measurements over North Africa (top left) and model results from MERRA-1, CRTM, and MOPSMAP. Results of several CRTM and MOPSMAP model runs are shown (see individual figure titles for details).
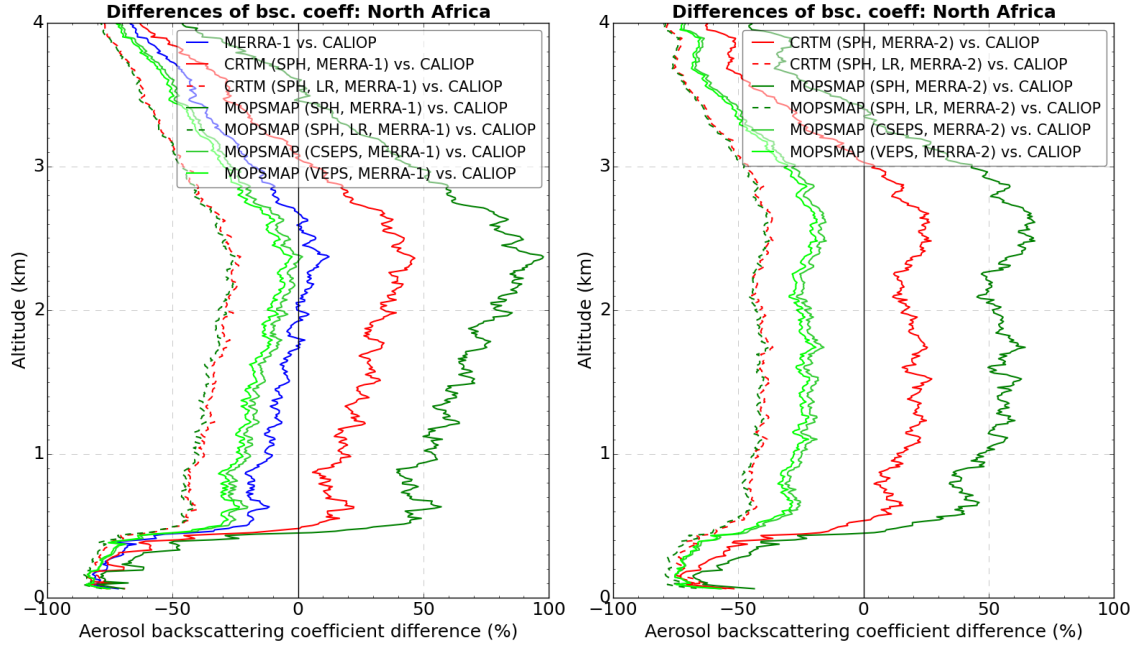
Figure 15: Model minus observation backscattering coefficient difference profiles over Africa from different model simulations. Results are shown for MERRA-1 (left) and MERRA-2 (right) input data.

MOPSMAP(SPH, MERRA-1) are in better agreement. Figure 17 reveals that all models exhibit a systematical negative bias with the smallest bias found for CRTM and largest for MERRA-1. For MERRA-2, mean model biases are about -50 % for CRTM and -60 % for MOPSMAP. Differences between the three MOPSMAP simulations are negligible because of the absence of dust in this region.

Figures 18 and 19 show validation results of backscattering coefficients above the North Atlantic. Contrary to the African results, there is hardly any difference between the simulation using backscattering information from the aerosol look-up tables or assuming a constant LIDAR ratio. This indicates a better LIDAR ratio parameterization for sea salt than for dust. Vertical difference profiles of backscattering coefficients are similar to difference profiles of extinction coefficients with negative biases for all simulations almost everywhere. Smallest biases are again found for CRTM, largest biases for MERRA-1.
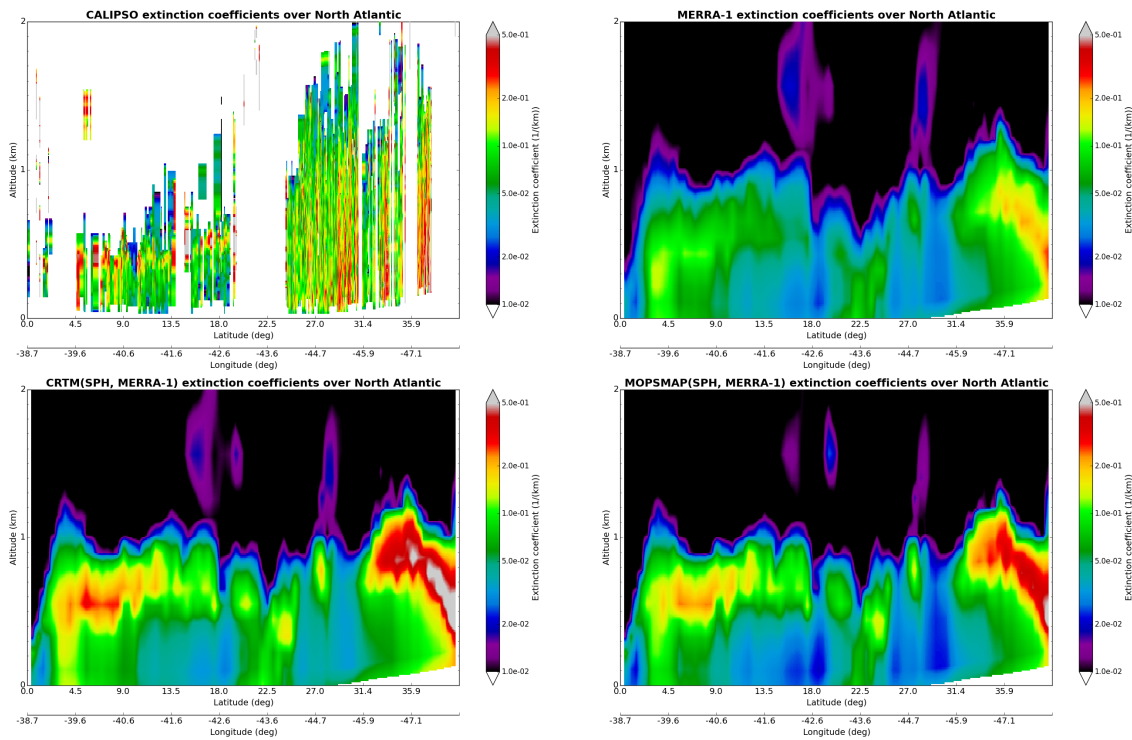
Figure 16: Vertically-resolved extinction coefficients from CALIPSO measurements on 17 April 2010 over the North Atlantic (top left) and model results from MERRA-1, CRTM(SPH, MERRA-1), and MOPSMAP(SPH, MERRA-1).
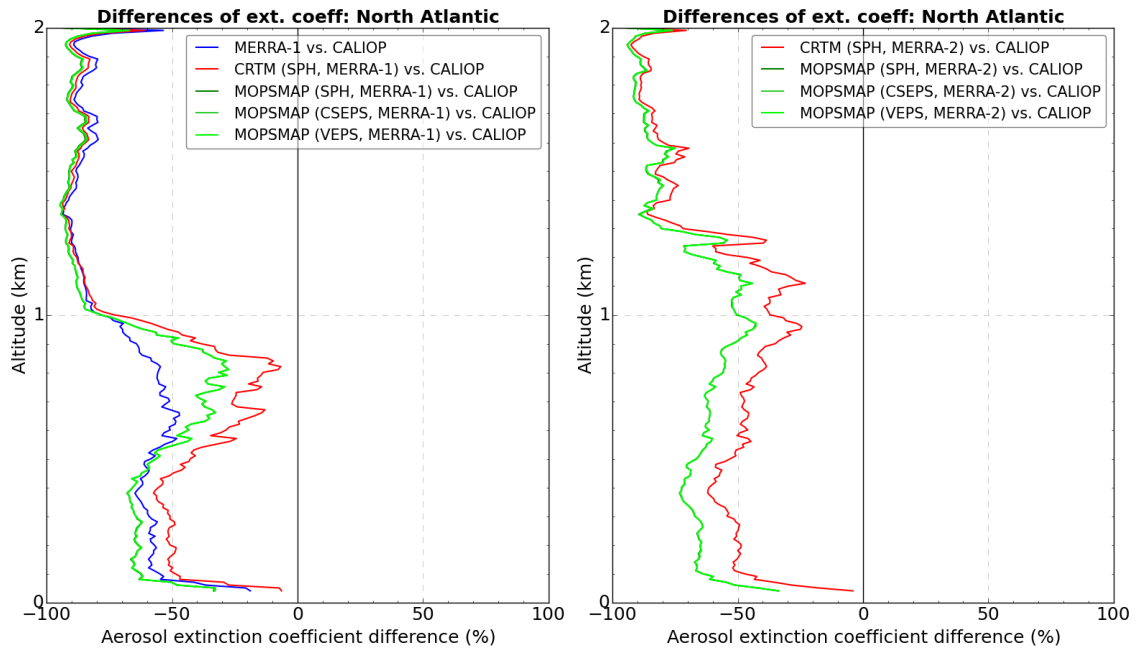
Figure 17: Model minus observation extinction coefficient difference profiles over the North Atlantic from different model simulations. Results are shown for MERRA-1 (left) and MERRA-2 (right) input data.

5. Summary, conclusions, and outlook

This report gave detailed information about modeling AOP with CRTM. Furthermore, model results were validated with another aerosol model (MERRA) and with observations. The following results were obtained:

1. CRTM is now able to simulate aerosol extinction and backscattering coefficients as observed with LIDAR instruments; AOP can be simulated for all wavelengths that are typically used for LIDAR measurements (i.e., 355 nm, 532 nm, and 1064 nm);

2. Two aerosol look-up tables can be used for CRTM AOP simulations: an extended CRTM table and a table that is based on MOPSMAP;

3. The MOPSMAP look-up table also contains AOP of non-spherical dust particles;

4. Aerosol backscattering coefficients can be computed using (i) one of the aerosol look-up tables or (ii) aerosol extinction coefficients from one of the aerosol look-up tables and assuming a constant LIDAR ratio which is different for each aerosol type;

5. The comparison between CRTM simulations and MERRA reanalyses showed that the models are, in general, in good agreement;

6. Compared to MERRA reanalyses, CRTM AOD is larger over the oceans but smaller over regions with high dust load (such as over the Saharan region in Africa);
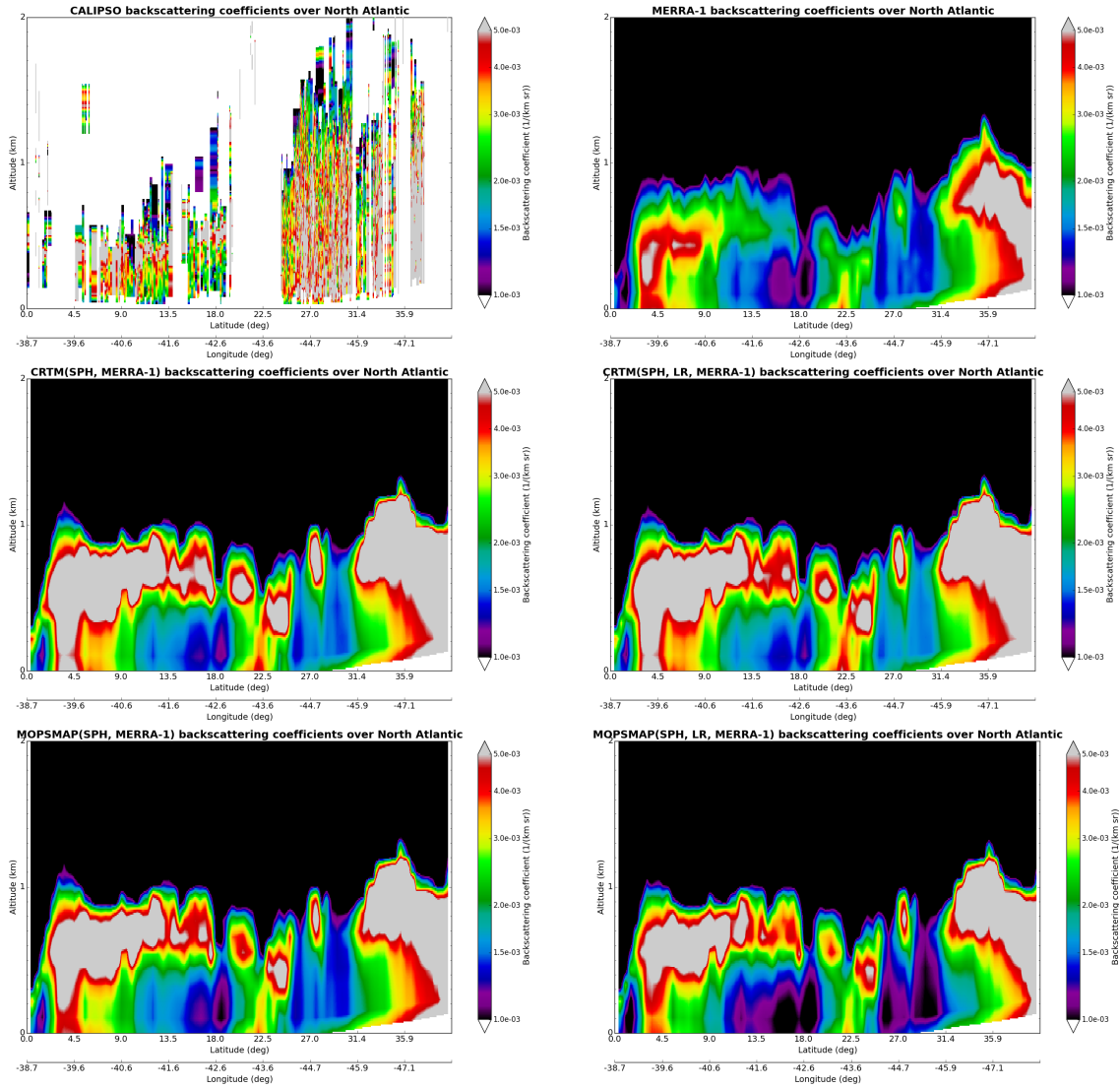
Figure 18: Vertically-resolved backscattering coefficients from CALIPSO measurements over the North Atlantic (top left) and model results from MERRA-1, CRTM, and MOPSMAP. Results of several CRTM and MOPSMAP model runs are shown (see individual figure titles for details).
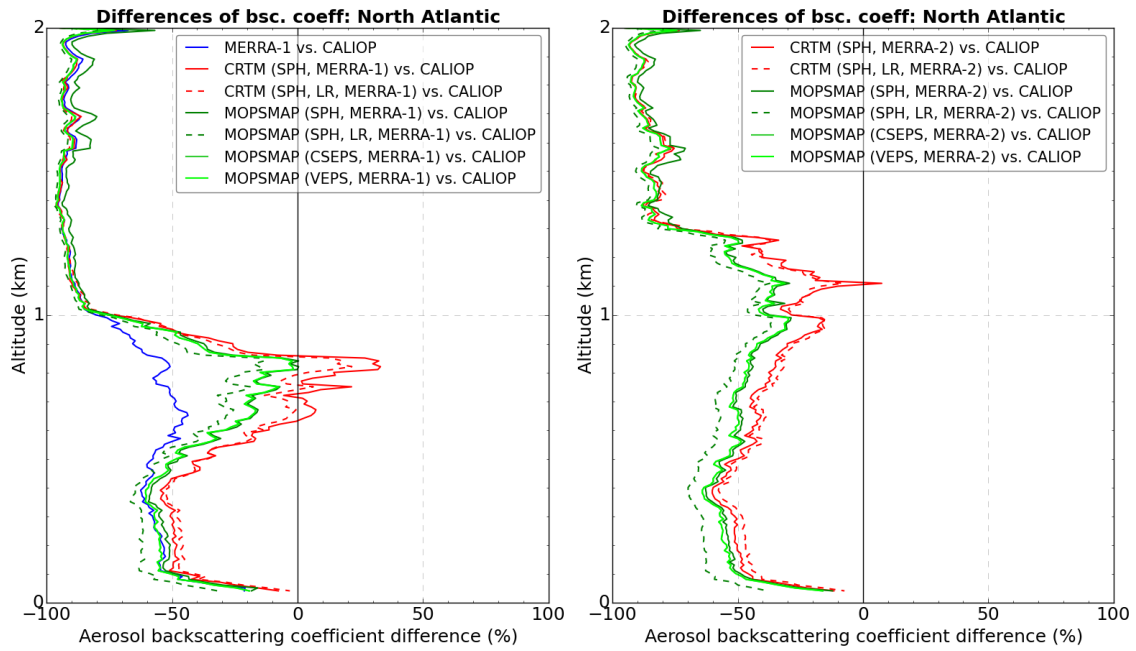
Figure 19: Model minus observation backscattering coefficient difference profiles over the North Atlantic from different model simulations. Results are shown for MERRA-1 (left) and MERRA-2 (right) input data.

7. Over dusty regions, AOD differences are reduced when non-spherical effects are accounted for;

8. Validation with AOD measurements from AERONET revealed only small model biases (which can, at least partly, be caused by biased aerosol concentrations rather than model AOP);

9. Vertical profiles of aerosol extinction and backscattering coefficients agree reasonably well for all models;

10. Over dusty regions, validation with AOP measurements from the CALIOP satellite revealed a negative bias (up to -40 %) of CRTM extinction coefficients (i.e., the model underestimates aerosol extinction);

11. Over the ocean, the CRTM model bias has similar magnitude

12. The bias of backscattering coefficients simulated with CRTM depends on how it is computed: if the simulation uses information of spherical aerosols of the aerosol look-up tables, CRTM overestimates backscattering coefficients over dusty regions; assuming a constant LR for individual aerosol types, simulated backscattering coefficients are too small over dusty regions; best results and smallest biases are obtained when simulating backscattering coefficients with non-spherical particles;

13. Over the ocean, simulated backscattering coefficients are similar for all model runs (i.e., influence of the calculation method is much smaller compared to the dusty region)

14. These results are encouraging to continue with part II of this project: the assimilation of vertically-resolved LIDAR measurements using an appropriate assimilation tool.

There is still quite some work left to successfully assimilate LIDAR measurements into an air quality model. This work includes further CRTM developments as well as the implementation into the data assimilation software.

Most important future CRTM developments include (i) the generation of a CRTM coefficient file for the CALIPSO satellite (so far, all tests were performed using the CRTM coefficient file of MODIS onboard the Aqua satellite), and (ii) testing the tangent linear and adjoint models. After this is done, the assimilation of aerosol extinction and backscattering coefficients can be implemented into an appropriate data assimilation tool.

LIDAR data assimilation can then be improved by implementing the observation operator of the attenuated backscattering signal. Rayleigh scattering as well as the absorption of radiation in the ultraviolet and visible parts of the spectrum by ozone, nitrogen dioxide, and sulfur dioxide (in the ultraviolet only) as well as in the infrared part of the spectrum by oxygen and carbon dioxide need to be accounted for. More information can be found in Sič (2014).

In recent years, spaceborne LIDAR-based measurements have only been performed by the CALIPSO satellite, launched in 2006. The satellite is aging, however, but there are other satellites performing similar LIDAR measurements. In August 2018, the Atmospheric Dynamics Mission–Aeolus (ADM-Aeolus) satellite has successfully been launched into orbit. When these data are publicly available, they can be also be assimilated into models. The implementation into CRTM, however, needs to be expanded in order to account for the angle of 35 degrees off-nadir, where measurements are performed. Earth Cloud Aerosol and Radiation Explorer (EarthCARE) (scheduled for launch in 2021) will also provide vertically-resolved LIDAR measurements that can be used to improve model forecasts.

Appendices

A. Reconstruction of CRTM backscattering coefficients

A.1. Legendre polynomials

If $P(x)$ is a function defined from $x = -1$ to $x = +1$, it can be written as

$$P(x) = c_0 \mathcal{L}_0(x) + c_1 \mathcal{L}_1(x) + c_2 \mathcal{L}_2(x) + \cdots = \sum_{n=0}^{\infty} c_n \mathcal{L}_n(x) \tag{38}$$

with c_n being some coefficients and $\mathcal{L}_n(x)$ being Legendre polynomials, i.e., orthogonal functions on $[-1, 1]$.

Legendre polynomials are given by

$$\mathcal{L}_0(x) = 1 \tag{39}$$
$$\mathcal{L}_1(x) = x \tag{40}$$
$$\mathcal{L}_{n+1}(x) = \frac{2n+1}{n+1} x \mathcal{L}_n(x) - \frac{n}{n+1} \mathcal{L}_{n-1}(x). \tag{41}$$

A.2. Clenshaw's recurrence formula

Clenshaw's recurrence formula can be used to efficiently evaluate a sum of coefficients times functions that obey a recurrence formula, e.g.,

$$P(x) = \sum_{i=0}^{i_{max}} k_i \phi_i(x), \tag{42}$$

with $\phi(x)$ satisfying the recurrence relation

$$\phi_{i+1}(x) = \alpha_i(x) \phi_i(x) + \beta_i(x) \phi_{i-1}(x) \tag{43}$$

for some functions $\alpha_i(x)$ and $\beta_i(x)$.

Now introduce the quantities $b_i(x)$ ($i = i_{max}, \ldots, 1$), defined by the following recurrence:

$$b_{i_{max}+2}(x) = 0 \tag{44}$$
$$b_{i_{max}+1}(x) = 0 \tag{45}$$
$$b_i(x) = \alpha_i(x) b_{i+1}(x) + \beta_{i+1}(x) b_{i+2}(x) + k_i \quad i = i_{max}, \ldots, 1. \tag{46}$$

Using Eq. (46) to get c_i

$$k_i = b_i(x) - \alpha_i(x) b_{i+1}(x) - \beta_{i+1}(x) b_{i+2}(x) \tag{47}$$

and writing out explicitly the sum given by Eq. (42) yields

$$P(x) = \ldots$$
$$+ \left[b_8(x) - \alpha_8(x)b_9(x) - \beta_9(x)b_{10}(x)\right]\phi_8(x)$$
$$+ \left[b_7(x) - \alpha_7(x)b_8(x) - \beta_8(x)b_9(x)\right]\phi_7(x)$$
$$+ \left[b_6(x) - \alpha_6(x)b_7(x) - \beta_7(x)b_8(x)\right]\phi_6(x)$$
$$+ \left[b_5(x) - \alpha_5(x)b_6(x) - \beta_6(x)b_7(x)\right]\phi_5(x)$$
$$+ \ldots$$
$$+ \left[b_2(x) - \alpha_2(x)b_3(x) - \beta_3(x)b_4(x)\right]\phi_2(x)$$
$$+ \left[b_1(x) - \alpha_1(x)b_2(x) - \beta_2(x)b_3(x)\right]\phi_1(x)$$
$$+ \left[b_0(x) - \alpha_0(x)b_1(x) - \beta_1(x)b_2(x)\right]\phi_0(x).$$

Since the last line of this expression seems to be

$$\left[b_0(x) - \alpha_0(x)b_1(x) - \beta_1(x)b_2(x)\right]\phi_0(x) = k_0(x)\phi_0(x)$$
$$= \left[k_0(x) + \beta_1(x)b_2(x) - \beta_1(x)b_2(x)\right]\phi_0(x).$$

the only surviving terms are

$$P(x) = \sum_{i=0}^{i_{\max}} k_i\phi_i(x) = \beta_1(x)b_2(x)\phi_0(x) + b_1(x)\phi_1(x) + k_0\phi_0(x). \tag{48}$$

Equations (44), (45), (46), and (48) are Clenshaw's recurrence formula, which can be used to evaluate Eq. (42).

A.3. Combined use of Legendre polynomials and Clenshaw's recurrence formula

Comparing Eqs. (41) and (43) yields

$$\phi_n(x) = \mathcal{L}_n(x), \tag{49}$$
$$\phi_0(x) = \mathcal{L}_0(x) = 1, \tag{50}$$
$$\phi_1(x) = \mathcal{L}_1(x) = x, \tag{51}$$
$$\alpha_n(x) = \frac{2n+1}{n+1}x, \tag{52}$$
$$\beta_n(x) = -\frac{n}{n+1}. \tag{53}$$

Comparison of Eq. (38) with the upper limit of the sum truncated at $n_{\max}$ and Eq. (42) yields

$$k_n = c_n, \tag{54}$$

which can be used to calculated $b_n(x)$ using Eq. (46):

$$b_n(x) = \frac{2n+1}{n+1}xb_{n+1}(x) - \frac{n+1}{n+2}b_{n+2}(x) + c_n. \tag{55}$$

Using Eq. (53) and evaluating $b_n(x)$ at $n = 1$ yields

$$\beta_1(x) = -\frac{1}{2}. \tag{56}$$

Using all these quantities and inserting them into Eq. (48) enables the reconstruction of the function $P(x)$, defined from $x = -1$ to $x = +1$ and expanded into some coefficients and Legendre polynomials:

$$P(x) = \sum_{n=0}^{n_{\text{max}}} c_n \mathcal{L}_n(x) = -\frac{1}{2}b_2(x) + xb_1(x) + c_0. \tag{57}$$

A.4. Reconstruction of backscattering coefficients

1. Evaluate the function $x = \cos\varphi$ at $x = -1$ (i.e., backscattering at $\varphi = \pi$).

2. Calculate the coefficients

$$n_1 = \frac{2n + 1}{n + 1} \tag{58}$$

$$n_2 = \frac{n + 1}{n + 2} \tag{59}$$

for $n = 1, \ldots n_{\text{max}}$ used in Eq. (55).

3. Use Eq. (55) with $b_{n_{\text{max}}+2} = b_{n_{\text{max}}+1} = 0$ (Eqs. (44) and (45)), $x = -1$ (step 1), the coefficients n_1 and n_2 (step 2), and the phase coefficients Acn and go through all b_n to calculate b_2 and b_1

$$b_n(x) = n_1 x b_{n+1}(x) - n_2 b_{n+2}(x) + c_n. \tag{60}$$

4. Use Eq. (57) with b_2, b_1, $x = -1$, and the phase coefficient c_0 to calculate the $P(\pi)$

5. Use Eq. (7) to calculate the mass backscattering coefficient: divide $P(\pi)$ by 4π and multiply it with the mass extinction coefficient κ_e and the single scatter albedo ω.

6. DONE!!

A.5. Example

Using four Legendre terms, the coefficients n_1 and n_2 are

$$n_1(1:4) = 1.50, 1.67, 1.75, 1.80$$
$$n_2(1:4) = 0.67, 0.75, 0.80, 0.83$$

At a wavelength of 550 nm and no humidity (i.e., smallest aerosol size), the phase coefficients c_n for all aerosol types are

$$c_{\text{dust}}(0:4) = 0.50, 0.74, 0.64, 0.11, 0.36$$
$$c_{\text{SSAM}}(0:4) = 0.50, 0.82, 0.68, 0.19, 0.31$$
$$c_{\text{SSCM1}}(0:4) = 0.50, 0.67, 0.61, 0.02, 0.45$$
$$c_{\text{SSCM2}}(0:4) = 0.50, 0.61, 0.50, -0.17, 0.60$$
$$c_{\text{SSCM3}}(0:4) = 0.50, 0.62, 0.44, -0.23, 0.66$$
$$c_{\text{OC}}(0:4) = 0.50, 0.80, 0.63, 0.21, 0.09$$
$$c_{\text{BC}}(0:4) = 0.50, 0.47, 0.40, 0.12, 0.27$$
$$c_{\text{sulf}}(0:4) = 0.50, 0.87, 0.72, 0.23, 0.33$$

Iterative calculation of b_2, b_1 for sulfate, e.g., yields

$$b_6 = 0.0$$
$$b_5 = 0.0$$
$$b_4 = 0.33$$
$$b_3 = -0.34$$
$$b_2 = 1.05$$
$$b_1 = -0.47$$

which yields 0.45 for the reconstructed phase function $P(\pi)$. For all aerosols, $P(\pi)$ is equal to

$$P_{\text{dust}}(\pi) = 0.66$$
$$P_{\text{SSAM}}(\pi) = 0.49$$
$$P_{\text{SSCM1}}(\pi) = 0.87$$
$$P_{\text{SSCM2}}(\pi) = 1.15$$
$$P_{\text{SSCM3}}(\pi) = 1.21$$
$$P_{\text{OC}}(\pi) = 0.21$$
$$P_{\text{BC}}(\pi) = 0.32$$
$$P_{\text{sulf}}(\pi) = 0.45$$

Mass backscattering coefficients κ_{b} are then obtained by

$$\kappa_{\text{b}} = \kappa_{\text{e}}\omega\frac{P(\pi)}{4\pi} \tag{61}$$

with the mass extinction coefficient κ_e and single scatter albedo ω. At 550 nm and no humidity, the dimensionless single scatter albedo w for all aerosol types is

$$\omega_{\text{dust}} = 0.98$$
$$\omega_{\text{SSAM}} = 1.00$$
$$\omega_{\text{SSCM1}} = 1.00$$
$$\omega_{\text{SSCM2}} = 1.00$$
$$\omega_{\text{SSCM3}} = 1.00$$
$$\omega_{\text{OC}} = 0.96$$
$$\omega_{\text{BC}} = 0.19$$
$$\omega_{\text{sulf}} = 1.00$$

the mass extinction coefficient is

$$\kappa_{e,\text{dust}} = 1318.0 \text{ m}^2 \text{ kg}^{-1}$$
$$\kappa_{e,\text{SSAM}} = 2588.0 \text{ m}^2 \text{ kg}^{-1}$$
$$\kappa_{e,\text{SSCM1}} = 898.1 \text{ m}^2 \text{ kg}^{-1}$$
$$\kappa_{e,\text{SSCM2}} = 235.5 \text{ m}^2 \text{ kg}^{-1}$$
$$\kappa_{e,\text{SSCM3}} = 97.1 \text{ m}^2 \text{ kg}^{-1}$$
$$\kappa_{e,\text{OC}} = 2649.0 \text{ m}^2 \text{ kg}^{-1}$$
$$\kappa_{e,\text{BC}} = 8962.0 \text{ m}^2 \text{ kg}^{-1}$$
$$\kappa_{e,\text{sulf}} = 3133.0 \text{ m}^2 \text{ kg}^{-1}$$

and finally, κ_b is

$$\kappa_{b,\text{dust}} = 67.63 \text{ m}^2 \text{ kg}^{-1} \text{ sr}^{-1}$$
$$\kappa_{b,\text{SSAM}} = 100.98 \text{ m}^2 \text{ kg}^{-1} \text{ sr}^{-1}$$
$$\kappa_{b,\text{SSCM1}} = 62.06 \text{ m}^2 \text{ kg}^{-1} \text{ sr}^{-1}$$
$$\kappa_{b,\text{SSCM2}} = 21.64 \text{ m}^2 \text{ kg}^{-1} \text{ sr}^{-1}$$
$$\kappa_{b,\text{SSCM3}} = 9.32 \text{ m}^2 \text{ kg}^{-1} \text{ sr}^{-1}$$
$$\kappa_{b,\text{OC}} = 43.43 \text{ m}^2 \text{ kg}^{-1} \text{ sr}^{-1}$$
$$\kappa_{b,\text{BC}} = 42.25 \text{ m}^2 \text{ kg}^{-1} \text{ sr}^{-1}$$
$$\kappa_{b,\text{sulf}} = 111.77 \text{ m}^2 \text{ kg}^{-1} \text{ sr}^{-1}$$

The LIDAR ratio S, which is also known as the extinction-to-backscatter ratio can be calculated as

$$S = \frac{\kappa_e}{\kappa_b} = \frac{4\pi}{wP(\pi)}. \tag{62}$$

At a wavelength of 550 nm and no humidity, it is equal to

$$S_{\text{dust}} = 19.49$$
$$S_{\text{SSAM}} = 25.63$$
$$S_{\text{SSCM1}} = 14.47$$
$$S_{\text{SSCM2}} = 10.88$$
$$S_{\text{SSCM3}} = 10.42$$
$$S_{\text{OC}} = 61.00$$
$$S_{\text{BC}} = 212.13$$
$$S_{\text{sulf}} = 28.03$$

for all aerosol types. Note that these numbers are slightly different than data stored in the new aerosol table because they were obtained using 16 Legendre coefficients instead of only 4. To give a better idea about the differences, these numbers are also given below

$$\kappa_{\text{b,dust}} = 33.08 \text{ m}^2 \text{kg}^{-1} \text{sr}^{-1}$$
$$\kappa_{\text{b,SSAM}} = 38.21 \text{ m}^2 \text{kg}^{-1} \text{sr}^{-1}$$
$$\kappa_{\text{b,SSCM1}} = 26.67 \text{ m}^2 \text{kg}^{-1} \text{sr}^{-1}$$
$$\kappa_{\text{b,SSCM2}} = 20.33 \text{ m}^2 \text{kg}^{-1} \text{sr}^{-1}$$
$$\kappa_{\text{b,SSCM3}} = 11.15 \text{ m}^2 \text{kg}^{-1} \text{sr}^{-1}$$
$$\kappa_{\text{b,OC}} = 25.86 \text{ m}^2 \text{kg}^{-1} \text{sr}^{-1}$$
$$\kappa_{\text{b,BC}} = 43.53 \text{ m}^2 \text{kg}^{-1} \text{sr}^{-1}$$
$$\kappa_{\text{b,sulf}} = 24.14 \text{ m}^2 \text{kg}^{-1} \text{sr}^{-1}$$

and

$$S_{\text{dust}} = 39.85$$
$$S_{\text{SSAM}} = 67.73$$
$$S_{\text{SSCM1}} = 33.68$$
$$S_{\text{SSCM2}} = 11.58$$
$$S_{\text{SSCM3}} = 8.71$$
$$S_{\text{OC}} = 102.43$$
$$S_{\text{BC}} = 205.89$$
$$S_{\text{sulf}} = 129.76$$

again, for a wavelength of 550 nm and no humidity.

B. Tangent linear and adjoint models of different AOP

Section 3.2 gave some background information about tangent linear and adjoint models and showed how to calculate these models for AOD. Here, I show how to calculate tangent linear and adjoint models for other AOP.

B.1. Volume extinction coefficient

In CRTM, the volume extinction coefficient β_e equals optical depth because all computations are performed for height/thickness independent quantities. It is modeled as

$$\beta_e = \chi \kappa_e, \tag{63}$$

with χ being the integrated aerosol concentration of a layer and κ_e the mass extinction coefficient, see also Section 3.1, Eq. (1). The derivations of the tangent linear statement and the adjoint model are identical to that of optical depth. The resulting tangent linear statement is

$$
\begin{aligned}
\delta\chi &= \delta\chi \\
\delta\kappa_e &= \delta\kappa_e \\
\delta\beta_e &= \kappa_e\delta\chi + \chi\delta\kappa_e
\end{aligned} \tag{64}
$$

and the adjoint model of β_e is

$$
\begin{aligned}
\delta\chi^\star &= \delta\chi^\star + \kappa_e\delta\beta_e^\star \\
\delta\kappa_e^\star &= \delta\kappa_e^\star + \chi\delta\beta_e^\star \\
\delta\beta_e^\star &= 0.
\end{aligned} \tag{65}
$$

B.2. Absorption coefficient

The absorption coefficient β_a can be obtained from the extinction coefficient β_e and single scatter albedo w and Eq. (4) because

$$
\begin{aligned}
(1-w) &= 1 - \frac{\beta_s}{\beta_s + \beta_a} \\
&= \frac{\beta_s + \beta_a - \beta_s}{\beta_s + \beta_a} \\
&= \frac{\beta_a}{\beta_s + \beta_a}
\end{aligned} \tag{66}
$$

$$\beta_a = (\beta_s + \beta_a)(1-w) = \beta_e(1-w). \tag{67}$$

The tangent linear statement is

$$
\begin{aligned}
\delta\beta_e &= \delta\beta_e \\
\delta w &= \delta w \\
\delta\beta_a &= \delta\beta_e(1-w) - \beta_e\delta w
\end{aligned} \tag{68}
$$

or

$$\begin{pmatrix} \delta\beta_\mathrm{e} \\ \delta w \\ \delta\beta_\mathrm{a} \end{pmatrix} = \begin{pmatrix} 1 & 0 & 0 \\ 0 & 1 & 0 \\ (1-w) & -\beta_\mathrm{e} & 0 \end{pmatrix} \begin{pmatrix} \delta\beta_\mathrm{e} \\ \delta w \\ \delta\beta_\mathrm{a} \end{pmatrix} \qquad (69)$$

in matrix notation.

The adjoint model of β_a can then be written as

$$\begin{pmatrix} \delta\beta_\mathrm{e}^\star \\ \delta w^\star \\ \delta\beta_\mathrm{a}^\star \end{pmatrix} = \begin{pmatrix} 1 & 0 & (1-w) \\ 0 & 1 & -\beta_\mathrm{e} \\ 0 & 0 & 0 \end{pmatrix} \begin{pmatrix} \delta\beta_\mathrm{e}^\star \\ \delta w^\star \\ \delta\beta_\mathrm{a}^\star \end{pmatrix}, \qquad (70)$$

which is equivalent to

$$\begin{aligned} \delta\beta_\mathrm{e}^\star &= \delta\beta_\mathrm{e}^\star + (1-w)\delta\beta_\mathrm{a}^\star \\ \delta w^\star &= \delta w^\star - \beta_\mathrm{e}\delta\beta_\mathrm{a}^\star \\ \delta\beta_\mathrm{a}^\star &= 0. \end{aligned} \qquad (71)$$

B.3. Volume scattering coefficient

In CRTM, volume scattering coefficient β_s is modeled as

$$\beta_\mathrm{s} = \chi\kappa_\mathrm{e}w, \qquad (72)$$

with χ being integrated aerosol concentration of a layer, κ_e the mass extinction coefficient, and w single scatter albedo, see also Section 3.1, Eq. (3). The tangent linear statement is

$$\begin{aligned} \delta\chi &= \delta\chi \\ \delta\kappa_\mathrm{e} &= \delta\kappa_\mathrm{e} \\ \delta w &= \delta w \\ \delta\beta_\mathrm{s} &= \delta\chi\kappa_\mathrm{e}w + \chi\delta\kappa_\mathrm{e}w + \chi\kappa_\mathrm{e}\delta w \end{aligned} \qquad (73)$$

or

$$\begin{pmatrix} \delta\chi \\ \delta\kappa_\mathrm{e} \\ \delta w \\ \delta\beta_\mathrm{s} \end{pmatrix} = \begin{pmatrix} 1 & 0 & 0 & 0 \\ 0 & 1 & 0 & 0 \\ 0 & 0 & 1 & 0 \\ \kappa_\mathrm{e}w & \chi w & \chi\kappa_\mathrm{e} & 0 \end{pmatrix} \begin{pmatrix} \delta\chi \\ \delta\kappa_\mathrm{e} \\ \delta w \\ \delta\beta_\mathrm{s} \end{pmatrix} \qquad (74)$$

in matrix notation.

The adjoint model of β_s can then be written as

$$\begin{pmatrix} \delta\chi^\star \\ \delta\kappa_\mathrm{e}^\star \\ \delta w^\star \\ \delta\beta_\mathrm{s}^\star \end{pmatrix} = \begin{pmatrix} 1 & 0 & 0 & \kappa_\mathrm{e}w \\ 0 & 1 & 0 & \chi w \\ 0 & 0 & 1 & \chi\kappa_\mathrm{e} \\ 0 & 0 & 0 & 0 \end{pmatrix} \begin{pmatrix} \delta\chi^\star \\ \delta\kappa_\mathrm{e}^\star \\ \delta w^\star \\ \delta\beta_\mathrm{s}^\star \end{pmatrix}, \qquad (75)$$

which is equivalent to

$$
\begin{aligned}
\delta\chi^\star &= \delta\chi^\star + \kappa_{\mathrm{e}} w \delta\beta_{\mathrm{s}}^\star \\
\delta\kappa_{\mathrm{e}}^\star &= \delta\kappa_{\mathrm{e}}^\star + \chi w \delta\beta_{\mathrm{s}}^\star \\
\delta w^\star &= \delta w^\star + \chi \kappa_{\mathrm{e}} \delta\beta_{\mathrm{s}}^\star \\
\delta\beta_{\mathrm{s}}^\star &= 0.
\end{aligned}
\tag{76}
$$

B.4. Volume backscattering coefficient

The volume backscattering coefficient β_{b} is obtained from

$$
\beta_{\mathrm{b}} = \chi\kappa_{\mathrm{b}}
\tag{77}
$$

with χ being integrated aerosol concentration of a layer and κ_{b} the mass extinction coefficient, see also Section 3.1, Eq. (8). The tangent linear statement is

$$
\begin{aligned}
\delta\chi &= \delta\chi \\
\delta\kappa_{\mathrm{b}} &= \delta\kappa_{\mathrm{b}} \\
\delta\beta_{\mathrm{b}} &= \delta\chi\kappa_{\mathrm{b}} + \chi\delta\kappa_{\mathrm{b}}
\end{aligned}
\tag{78}
$$

or

$$
\begin{pmatrix} \delta\chi \\ \delta\kappa_{\mathrm{b}} \\ \delta\beta_{\mathrm{b}} \end{pmatrix} =
\begin{pmatrix} 1 & 0 & 0 \\ 0 & 1 & 0 \\ \kappa_{\mathrm{b}} & \chi & 0 \end{pmatrix}
\begin{pmatrix} \delta\chi \\ \delta\kappa_{\mathrm{b}} \\ \delta\beta_{\mathrm{b}} \end{pmatrix}
\tag{79}
$$

in matrix notation.

The adjoint model of β_{b} can then be written as

$$
\begin{pmatrix} \delta\chi^\star \\ \delta\kappa_{\mathrm{b}}^\star \\ \delta\beta_{\mathrm{b}}^\star \end{pmatrix} =
\begin{pmatrix} 1 & 0 & \kappa_{\mathrm{b}} \\ 0 & 1 & \chi \\ 0 & 0 & 0 \end{pmatrix}
\begin{pmatrix} \delta\chi^\star \\ \delta\kappa_{\mathrm{e}}^\star \\ \delta\beta_{\mathrm{s}}^\star \end{pmatrix},
\tag{80}
$$

which is equivalent to

$$
\begin{aligned}
\delta\chi^\star &= \delta\chi^\star + \kappa_{\mathrm{b}} \delta\beta_{\mathrm{b}}^\star \\
\delta\kappa_{\mathrm{b}}^\star &= \delta\kappa_{\mathrm{b}}^\star + \chi \delta\beta_{\mathrm{b}}^\star \\
\delta\beta_{\mathrm{b}}^\star &= 0.
\end{aligned}
\tag{81}
$$

The volume backscattering coefficient β_{b} can also be obtained by assuming a constant LIDAR ratio S

$$
\beta_{\mathrm{b}} \approx \frac{\beta_{\mathrm{e}}}{S}
\tag{82}
$$

with β_{e} being the volume extinction coefficient, see also Section 3.1, Eq. (12).

In this case, the tangent linear statement is

$$
\begin{aligned}
\delta\beta_{\mathrm{e}} &= \delta\beta_{\mathrm{e}} \\
\delta S &= 0 \\
\delta\beta_{\mathrm{b}} &= \delta\beta_{\mathrm{e}}
\end{aligned}
\tag{83}
$$

or

$$
\begin{pmatrix} \delta\beta_{\mathrm{e}} \\ \delta S \\ \delta\beta_{\mathrm{b}} \end{pmatrix} =
\begin{pmatrix} 1 & 0 & 0 \\ 0 & 0 & 0 \\ 1 & 0 & 0 \end{pmatrix}
\begin{pmatrix} \delta\beta_{\mathrm{e}} \\ \delta S \\ \delta\beta_{\mathrm{b}} \end{pmatrix}
\tag{84}
$$

in matrix notation.

The adjoint model of β_{b} can then be written as

$$
\begin{pmatrix} \delta\beta_{\mathrm{e}}^{\star} \\ \delta S^{\star} \\ \delta\beta_{\mathrm{b}}^{\star} \end{pmatrix} =
\begin{pmatrix} 1 & 0 & 1 \\ 0 & 0 & 0 \\ 0 & 0 & 0 \end{pmatrix}
\begin{pmatrix} \delta\beta_{\mathrm{e}}^{\star} \\ \delta S^{\star} \\ \delta\beta_{\mathrm{b}}^{\star} \end{pmatrix} ,
\tag{85}
$$

which is equivalent to

$$
\begin{aligned}
\delta\beta_{\mathrm{e}}^{\star} &= \delta\beta_{\mathrm{e}}^{\star} + \delta\beta_{\mathrm{b}}^{\star} \\
\delta S^{\star} &= 0 \\
\delta\beta_{\mathrm{b}}^{\star} &= 0.
\end{aligned}
\tag{86}
$$

Table 3: MERRA data used for CRTM computations, their description and units.

MERRA variable	description	unit
`lon`	longitude	`degrees_east`
`lat`	latitude	`degrees_north`
`lev`	layer	`layer`
`time`	time	`minutes since YYYY-MM-DD HH:MM:SS`
`ps/PS`	surface pressure	`Pa`
`delp/DELP`	pressure thickness	`Pa`
`RH`	relative humidity	`1`
`AIRDENS`	air density	$kg\,m^{-3}$
`du001/DU001`	dust mixing ratio (bin 1)	$kg\,kg^{-1}$
`du002/DU002`	dust mixing ratio (bin 2)	$kg\,kg^{-1}$
`du003/DU003`	dust mixing ratio (bin 3)	$kg\,kg^{-1}$
`du004/DU004`	dust mixing ratio (bin 4)	$kg\,kg^{-1}$
`du005/DU005`	dust mixing ratio (bin 5)	$kg\,kg^{-1}$
`ss001/SS001`	sea salt mixing ratio (bin 1)	$kg\,kg^{-1}$
`ss002/SS002`	sea salt mixing ratio (bin 2)	$kg\,kg^{-1}$
`ss003/SS003`	sea salt mixing ratio (bin 3)	$kg\,kg^{-1}$
`ss004/SS004`	sea salt mixing ratio (bin 4)	$kg\,kg^{-1}$
`ss005/SS005`	sea salt mixing ratio (bin 5)	$kg\,kg^{-1}$
`SO4`	sulfate aerosols	$kg\,kg^{-1}$
`BCphobic/BCPHOBIC`	hydrophobic BC	$kg\,kg^{-1}$
`BCphilic/BCPHILIC`	hydrophilic BC	$kg\,kg^{-1}$
`OCphobic/OCPHOBIC`	hydrophobic OC	$kg\,kg^{-1}$
`OCphilic/OCPHILIC`	hydrophilic OC	$kg\,kg^{-1}$

C. MERRA data preparation for CRTM

C.1. List of variables

The list of variables kept for further computations is given in Table 3.

C.2. Pressure and temperature from MERRA data

Vertical pressure profiles p are calculated from pressure thickness dp (accumulation of individual contributions of each layer). Temperature T is then obtained from pressure and density ϱ using the ideal gas law:

$$T = \frac{p}{\varrho R_{\mathrm{air}}} \tag{87}$$

with $R_{\mathrm{air}} = 287 \text{ J K}^{-1}\,\text{kg}^{-1}$ being the gas constant of dry air.

C.3. Unit conversion of aerosol concentrations

Due to CRTM input data requirements, MERRA aerosol mixing ratios ζ in $\mathrm{kg\,kg^{-1}}$ need to be converted to integrated aerosol concentrations for a layer χ in $\mathrm{kg\,m^{-2}}$. This was done using the hydrostatic equation in differential form:

$$\mathrm{d}p = p_\mathrm{top} - p_\mathrm{bottom} = -\varrho g \mathrm{d}z \tag{88}$$

($g = 9.81$ is the gravitational acceleration and $\mathrm{d}z$ the layer thickness) which yields

$$\mathrm{d}z = -\frac{\mathrm{d}p}{\varrho g} \tag{89}$$

and

$$\varrho \mathrm{d}z = -\frac{\mathrm{d}p}{g}. \tag{90}$$

Therefore,

$$[\zeta \varrho \mathrm{d}z] = \frac{\mathrm{kg}}{\mathrm{kg}} \frac{\mathrm{kg}}{\mathrm{m}^3} \, \mathrm{m} = \frac{\mathrm{kg}}{\mathrm{m}^2} = \left[-\zeta \frac{\mathrm{d}p}{g} \right] = [\chi]$$

The conversion factor therefore is $-\mathrm{d}p/g$. Note that the conversion factor depends on location and time.

List of Figures

List of Tables

Acronyms

3DVar 3-Dimensional Variational

4DVar 4-Dimensional Variational

ADM-Aeolus Atmospheric Dynamics Mission–Aeolus

AERONET AErosol RObotic NETwork

AOD Aerosol Optical Depth

AOP Aerosol Optical Properties

BC Black Carbon

CALIOP Cloud-Aerosol Lidar with Orthogonal Polarisation

CALIPSO Cloud-Aerosol Lidar and Infrared Pathfinder Satellite Observations

CIRES Cooperative Institute for Research in Environmental Sciences

CRTM Community Radiative Transfer Model

CSEPS Cross-Section Equivalent Prolate Spheriods

CU Colorado University

DTC Developmental Testbed Center

EarthCARE Earth Cloud Aerosol and Radiation Explorer

ESRL Earth System Research Laboratory

FGAT First Guess at Appropriate Time

GADS Global Aerosol Data Set

GEOS-5 Goddard Earth Observing System Data Assimilation System version 5

GOCART Global Ozone Chemistry Aerosol Radiation and Transport

GSD Global Systems Division

GSI Gridpoint Statistical Interpolation

JCSDA Joint Center for Satellite Data Assimilation

LIDAR LIght Detection And Ranging

LR LIDAR Ratio

MERRA Modern Era Retrospective-analysis for Research and Applications

MERRAero MERRA Aerosol Reanalysis

MODIS Moderate Resolution Imaging Spectroradiometer

MOPSMAP Modeled Optical Properties of enSeMbles of Aerosol Particles

NASA National Aeronautics and Space Administration

NOAA National Oceanic and Atmospheric Administration

OC Organic Carbon

SPH SPHerical

SSAM Sea Salt Accumulation Mode

SSCM Sea Salt Coarse Mode

Suomi-NPP Suomi National Polar-orbiting Partnership

UCAR University Corporation for Atmospheric Research

VEPS Volume-Equivalent Prolate Spheriods

VIIRS Visible Infrared Imaging Radiometer Suite

ZAMG Zentralanstalt für Meteorologie und Geodynamik

Bibliography

A. Benedetti, J.-J. Morcrette, O. Boucher, A. Dethof, R. J. Engelen, M. Fisher, H. Flentje, N. Huneeus, L. Jones, J. W. Kaiser, S. Kinne, A. Mangold, M. Razinger, A. J. Simmons, and M. Suttie. Aerosol analysis and forecast in the European Centre for Medium-Range Weather Forecasts Integrated Forecast System: 2. Data assimilation. *J. Geophys. Res.*, 114:D13205, 2009. doi: 10.1029/2008JD011115.

F. S. Binkowski and S. J. Roselle. Models-3 Community Multiscale Air Quality (CMAQ) model aerosol component: 1. Model description. *J. Geophys. Res.*, 108(D6), 2003. doi: 10.1029/2001JD001409.

S. P. Burton, R. A. Ferrare, M. A. Vaughan, A. H. Omar, R. R. Rogers, C. A. Hostetler, and J. W. Hair. Aerosol classification from airborne HSRL and comparisons with the CALIPSO vertical feature mask. *Atmospheric Measurement Techniques*, 6:1397–1412, 2013. doi: 10.5194/amt-6-1397-2013.

M. Chin, P. Ginoux, S. Kinne, O. Torres, B. N. Holben, B. N. Duncan, R. V. Martin, J. A. Logan, A. Higurashi, and T. Nakajima. Tropospheric aerosol optical thickness from the GOCART model and comparisons with satellite and sun photometer measurements. *J. Atmos. Sci.*, 59:461–483, 2000.

G. A. d'Almeida, P. Koepke, and E. P. Shettle. *Atmospheric Aerosols: Global Climatology and Radiative Characteristics*. A. Deepak Publishing, 1991.

J. Gasteiger and M. Wiegner. MOPSMAP v1.0: a versatile tool for the modeling of aerosol optical properties. *Geosci. Model Dev.*, 11:2739–2762, 2018. doi: 10.5194/gmd-11-2739-2018.

A. Geisinger, A. B. V. W. J. Strohbach, J. Förstner, and R. Potthast. Development and application of a backscatter lidar forward operator for quantitative validation of aerosol dispersion models and future data assimilation. *Atmospheric Measurement Techniques*, 10:4705–4726, 2017. doi: 10.5194/amt-10-4705-2017.

Q. S. He, C. C. Li, J. T. Mao, A. K. H. Lau, and P. R. Li. A study on the aerosol extinction-to-backscatter ratio with combination of micro-pulse LIDAR and MODIS over Hong Kong. *Atmos. Chem. Phys.*, 6(11):3243–3256, 2006. doi: 10.5194/acp-6-3243-2006.

M. Hess, P. Koepke, and I. Schult. Optical properties of aerosols and clouds: The software package OPAC. *Bull. Amer. Meteor. Soc.*, 79(5):831–844, 1998. doi: 10.1175/1520-0477(1998)079⟨0831:OPOAAC⟩2.0.CO;2.

K. Kandler, L. Schütz, C. Deutscher, M. Ebert, H. Hofmann, S. Jäckel, R.Jaenicke, P. Knippertz, K. Lieke, A. Massling, A. Petzold, A. Schladitz, B. Weinzierl, A. Wiedensohler, S. Zorn, and S. Weinbruch. Size distribution, mass concentration,

chemical and mineralogical composition and derived optical parameters of the boundary layer aerosol at Tinfou, Morocco, during SAMUM 2006. *Tellus B: Chemical and Physical Meteorology*, 61(1):32–50, 2009. doi: 10.1111/j.1600-0889.2008.00385.x.

P. Koepke, M. Hess, I. Schult, and E. P. Shettle. Global aerosol dataset. Technical report, Max-Plank-Institut fÃ¼r Meteorologie, Hamburg, Germany, 1997. Report No. 243.

Z. Liu, Q. Liu, H.-C. Lin, C. S. Schwartz, Y.-H. Lee, and T. Wang. Three-dimensional variational assimilation of MODIS aerosol optical depth: Implementation and application to a dust storm over East Asia. *J. Geophys. Res.*, 116:D23206, 2011. doi: 10.1029/2011JD016159.

M. Pagowski, Z. Liu, G. A. Grell, M. Hu, H.-C. Lin, and C. S. Schwartz. Implementation of aerosol assimilation in Gridpoint Statistical Interpolation (v. 3.2) and WRF-Chem (v. 3.4.1). *Geosci. Model Dev.*, 7:1621–1627, 2014. doi: 10.5194/gmd-7-1621-2014.

A. T. Prata, S. A. Young, S. T. Siems, and M. J. Manton. Lidar ratios of stratospheric volcanic ash and sulfate aerosols retrieved from CALIOP measurements. *Atmos. Chem. Phys.*, 17(13):8599–8618, 2017. doi: 10.5194/acp-17-8599-2017.

C. S. Schwartz, Z. Liu, H.-C. Lin, and S. A. McKeen. Simultaneous three-dimensional variational assimilation of surface fine particulate matter and MODIS aerosol optical depth. *J. Geophys. Res.*, 117:D13202, 2012. doi: 10.1029/2011JD017383.

B. Sič. Improvement of aerosol representation in a chemical-transport model: Modelling and data assimilation, 2014.

B. Sič, L. El Amraoui, A. Piacentini, V. Marécal, E. Emili, D. Cariolle, M. Prather, and J.-L. Attié. Aerosol data assimilation in the chemical transport model MOCAGE during the TRAQA/ChArMEx campaign: aerosol optical depth. *Atmospheric Measurement Techniques*, 9:5535–5554, 2016. doi: 10.5194/amt-9-5535-2016.

Y. Wang, K. N. Sartelet, M. Bocquet, P. Chazette, M. Sicard, G. D'Amico, J. F. Léon, L. Alados-Arboledas, A. Amodeo, P. Augustin, J. Bach, L. Belegante, I. Binietoglou, X. Bush, A. Comerón, H. Delbarre, D. Garcí-Vízcaino, J. L. Guerrero-Rascado, M. Hervo, M. Iarlori, P. Kokkalis, D. Lange, F. Molero, N. Montoux, A. M. noz, C. M. noz, D. Nicolae, A. Papayannis, G. Pappalardo, J. Preissler, V. Rizi, F. Rocadenbosch, K. Sellegri, F. Wagner, and F. Dulac. Assimilation of lidar signals: application to aerosol forecasting in the western Mediterranean basin. *Atmos. Chem. Phys.*, 14(22):12031–12053, 2014. doi: 10.5194/acp-14-12031-2014.

K. Yumimoto, I. Uno, N. Sugimoto, A. Shimizu, Z. Liu, and D. M. Winker. Adjoint inversion modeling of Asian dust emission using lidar observations. *Atmos. Chem. Phys.*, 8:2869–2884, 2008. doi: 10.5194/acp-8-2869-2008.

J. Zhang, J. S. Reid, D. L. Westphal, N. L. Baker, and E. J. Hyer. A system for operational aerosol optical depth data assimilation over global oceans. *J. Geophys. Res.*, 113:D10208, 2008. doi: 10.1029/2007JD009065.

J. Zhang, J. R. Campbell, J. S. Reid, D. L. Westphal, N. L. Baker, W. F. Campbell, and E. J. Hyer. Evaluating the impact of assimilating CALIOP-derived aerosol extinction profiles on a global mass transport model. *Geophys. Res. Lett.*, 38:L14801, 2011. doi: 10.1029/2011GL047737.

P. Zieger, R. Fierz-Schmidhauser, E. Weingartner, and U. Baltensperger. Effects of relative humidity on aerosol light scattering: results from different European sites. *Atmos. Chem. Phys.*, 13:10609–10631, 2013. doi: 10.5194/acp-13-10609-2013.